Transport and Confinement of Plumes from Tropopause-Overshooting Convection over the Contiguous United States During the Warm Season

Kai-Wei Chang[1], Kenneth P. Bowman[1], and Anita D. Rapp[1]

[1]Texas A&M University

November 24, 2022

Abstract

Tropopause-penetrating overshooting convection (OC) can transport tropospheric air into and affect the composition of the lower stratosphere. During the warm season, OC occurs frequently over the contiguous United States, and the transport of plumes from these events is modulated by the flow over North America, which throughout June to August is characterized by a large-scale anticyclone in the upper troposphere and lower stratosphere. This study uses data from the Next Generation Weather Radar (NEXRAD) and the ERA5 reanalysis to locate OC during May–August of 2008 to 2020. Evidence of convective transport is found well above the 380 K isentrope, which is the top of the "lowermost stratosphere" and also the top of the stratospheric middleworld. By initializing massless particles within the volume of OC above the tropopause, we perform trajectory calculations to simulate the transport of OC plumes. With three-dimensional diabatic trajectory modeling in isentropic coordinates using winds from ERA5, we quantify the confinement within the anticyclone and the number of trajectories transported into the tropical and extratropical stratosphere. By evaluating the trajectory residence time in the North American region, we find that July exhibits the strongest confinement, with about a quarter of trajectories staying in the region for more than 11 days. It is shown that, together with sufficient injection height, convective injection that occurs south of the jet and/or into anticyclonic regimes increases the chances of air remaining in the stratosphere. After 30 days, 45% of all air masses injected above the tropopause remain in the global stratosphere.

Figure 1.

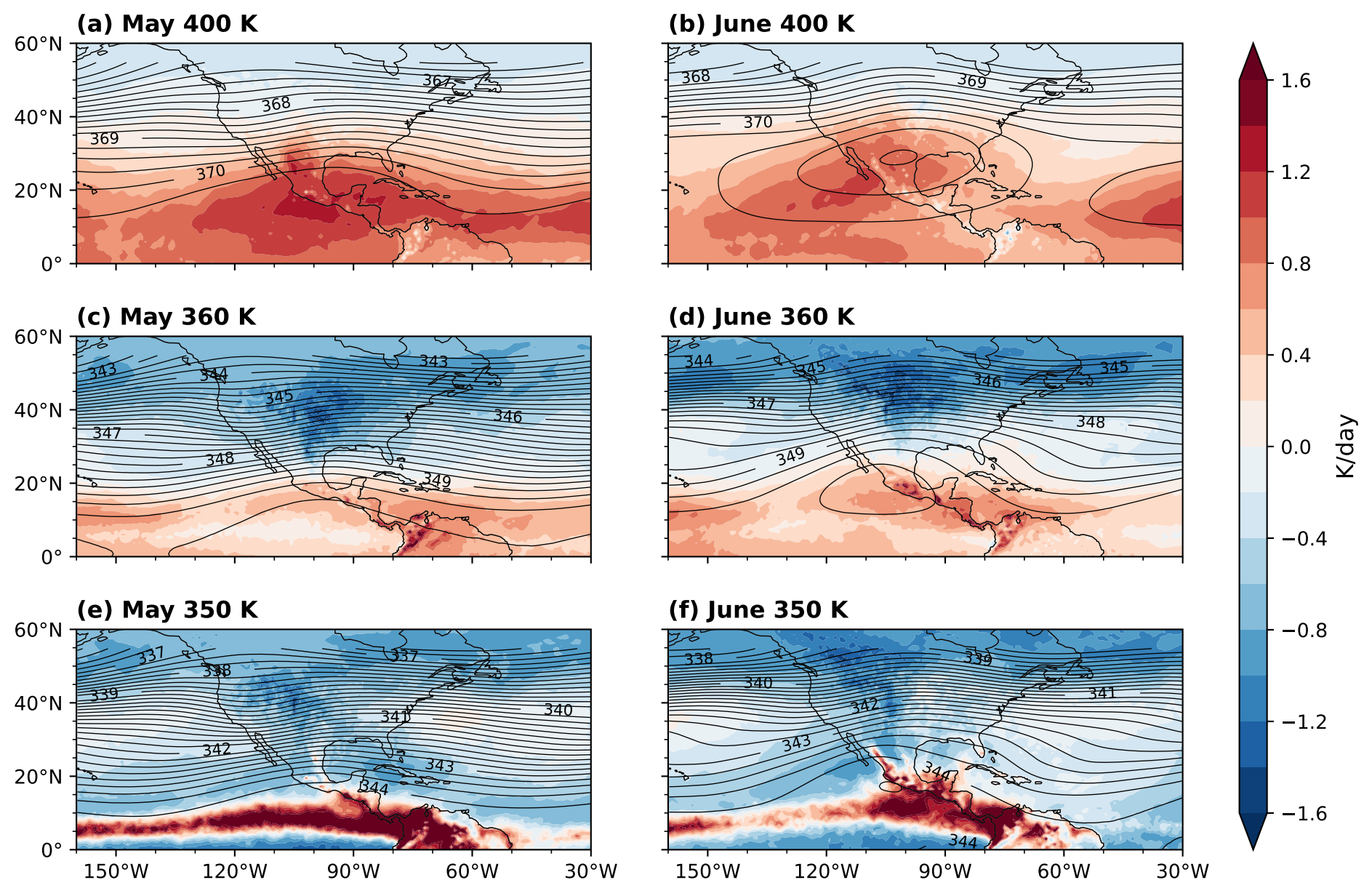
(a) May 400 K
(b) June 400 K
(c) May 360 K
(d) June 360 K
(e) May 350 K
(f) June 350 K
60°N
40°N
20°N
0°
150°W
120°W
90°W
60°W
30°W
K/day
1.6
1.2
0.8
0.4
0.0
−0.4
−0.8
−1.2
−1.6

Figure 2.

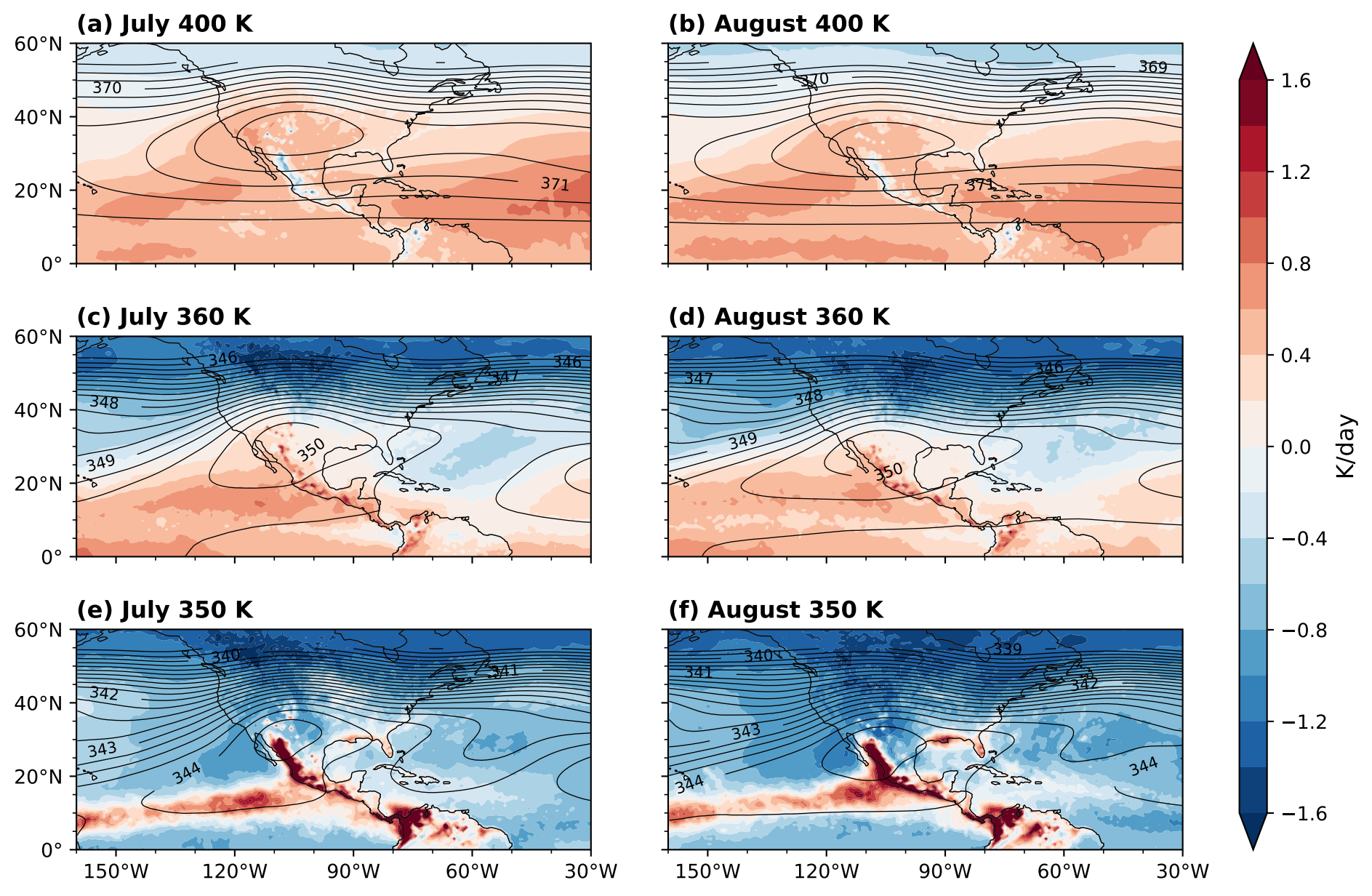
(a) July 400 K
(b) August 400 K
(c) July 360 K
(d) August 360 K
(e) July 350 K
(f) August 350 K
60°N
40°N
20°N
0°
150°W
120°W
90°W
60°W
30°W
370
371
369
346
347
348
349
350
340
341
342
343
344
339
1.6
1.2
0.8
0.4
0.0
−0.4
−0.8
−1.2
−1.6
K/day

Figure 3.

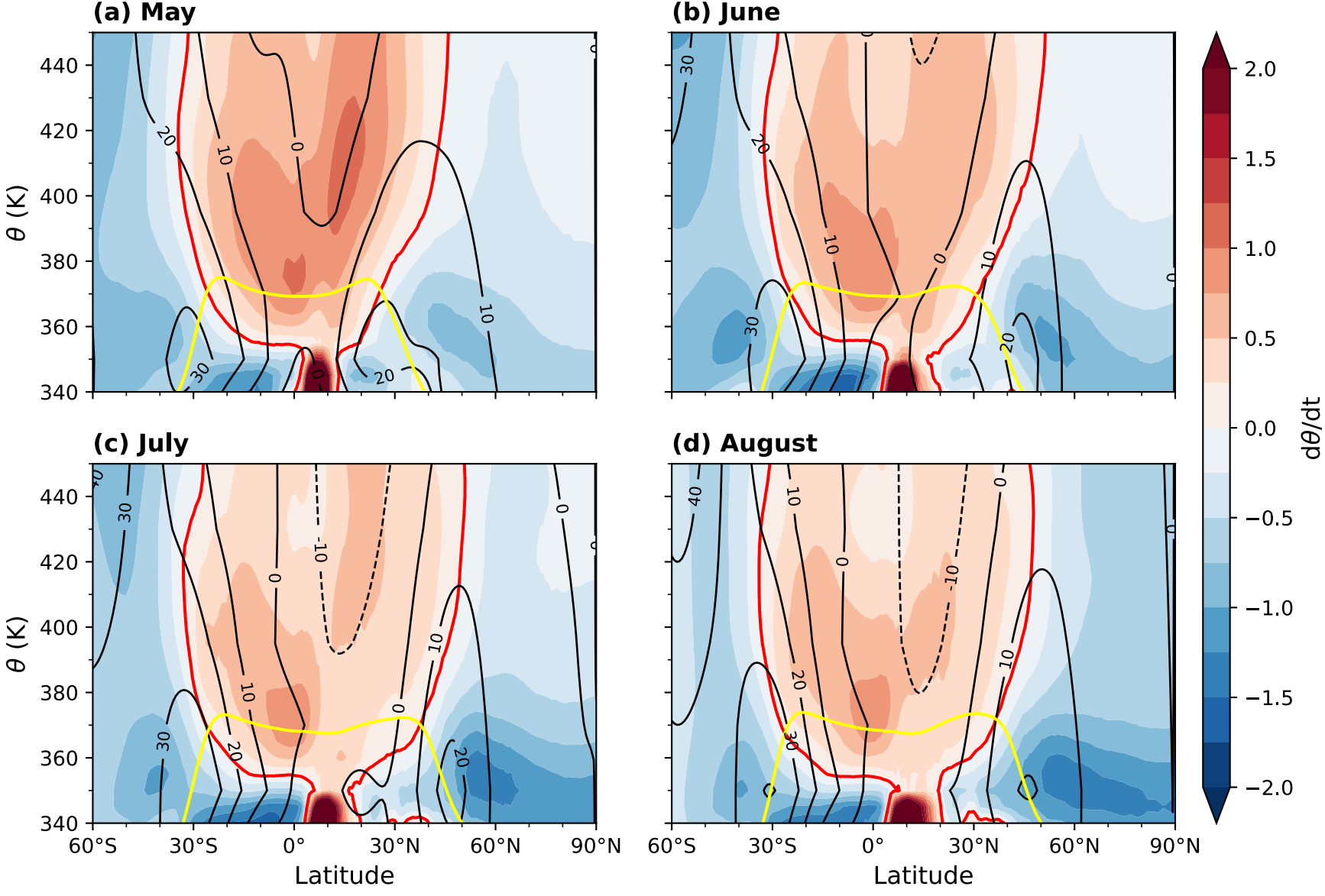
(a) May
(b) June
(c) July
(d) August
θ (K)
440
420
400
380
360
340
60°S
30°S
0°
30°N
60°N
90°N
Latitude
dθ/dt
2.0
1.5
1.0
0.5
0.0
−0.5
−1.0
−1.5
−2.0

Figure 4.

Total number of trajectories

Number of trajectories with residence time above 75th percentile

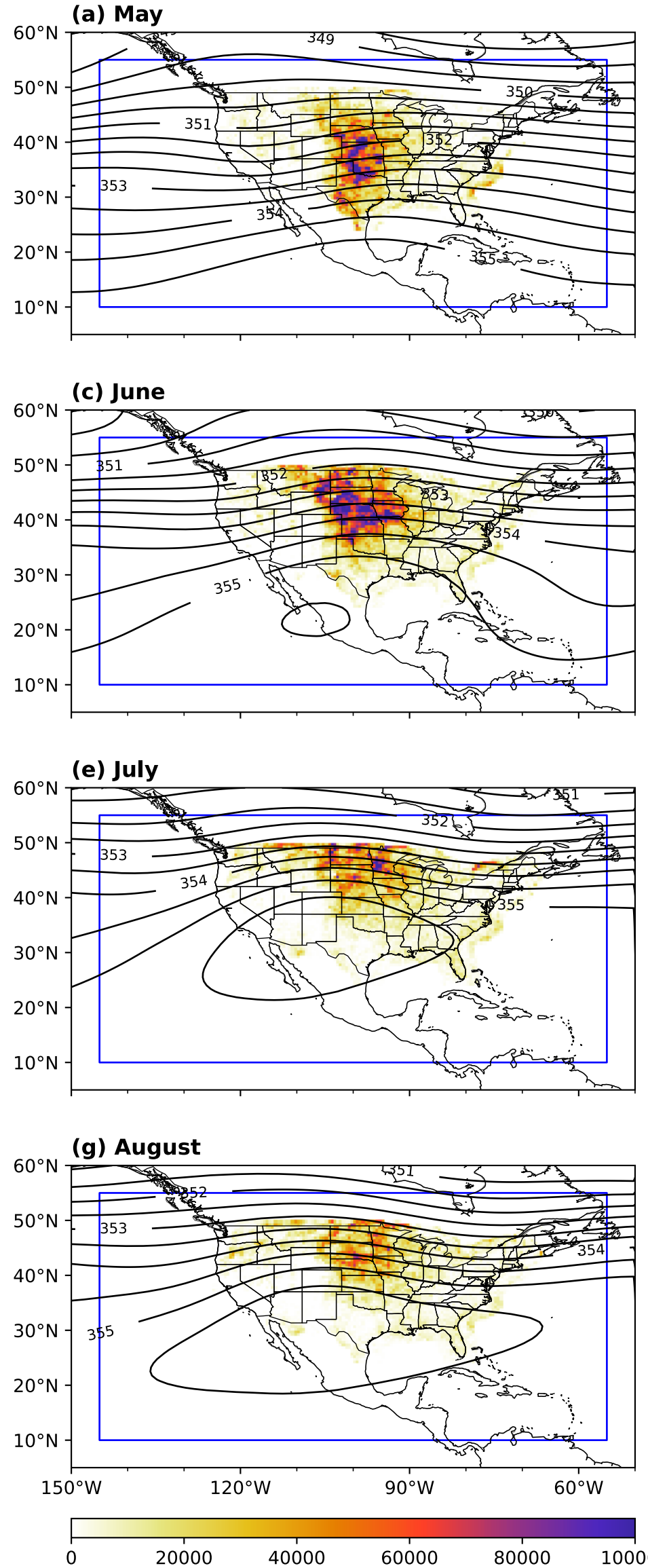

Figure 5.

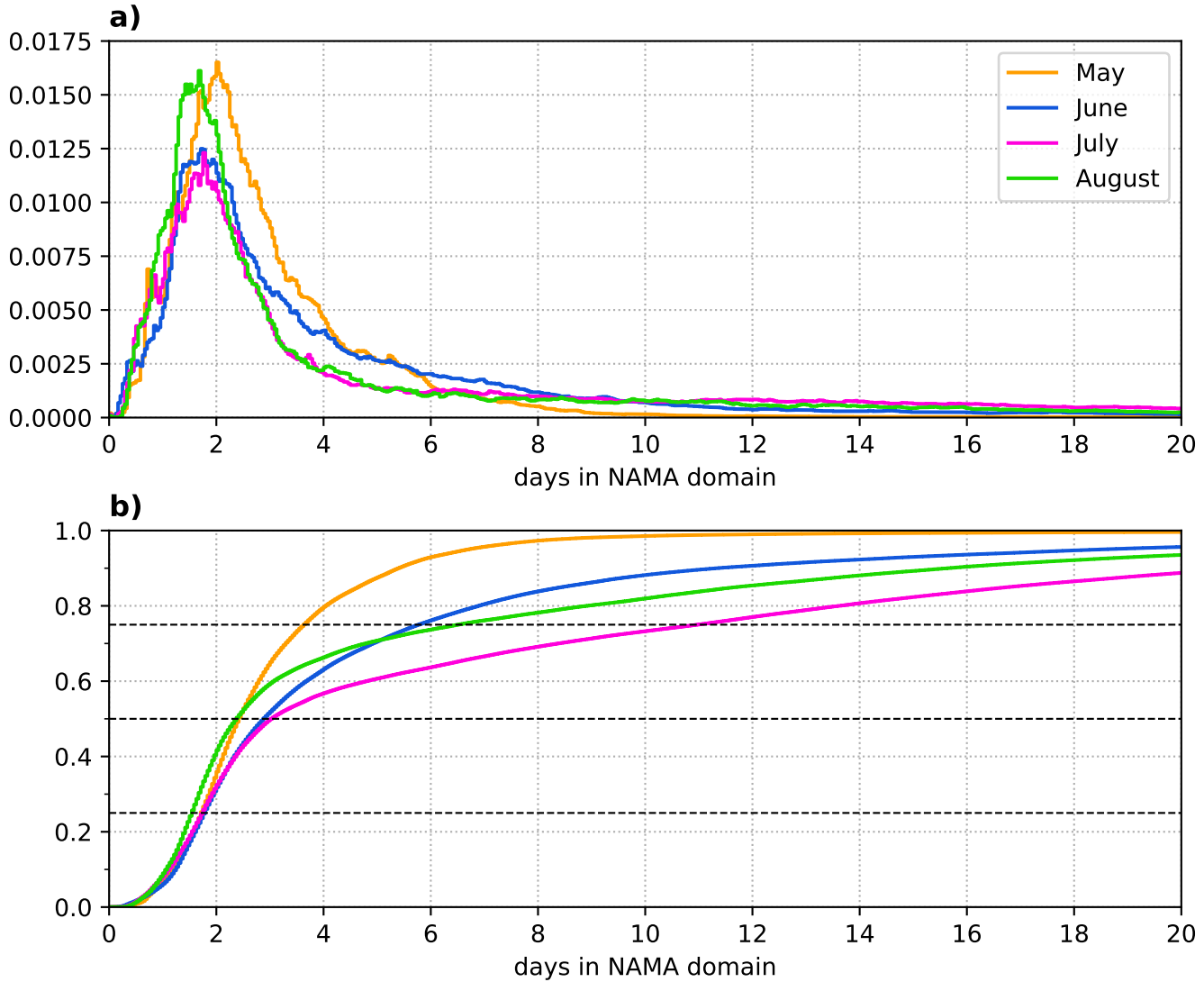
a)
0.0175
0.0150
0.0125
0.0100
0.0075
0.0050
0.0025
0.0000
0
2
4
6
8
10
12
14
16
18
20
days in NAMA domain
May
June
July
August
b)
1.0
0.8
0.6
0.4
0.2
0.0
0
2
4
6
8
10
12
14
16
18
20
days in NAMA domain

Figure 6.

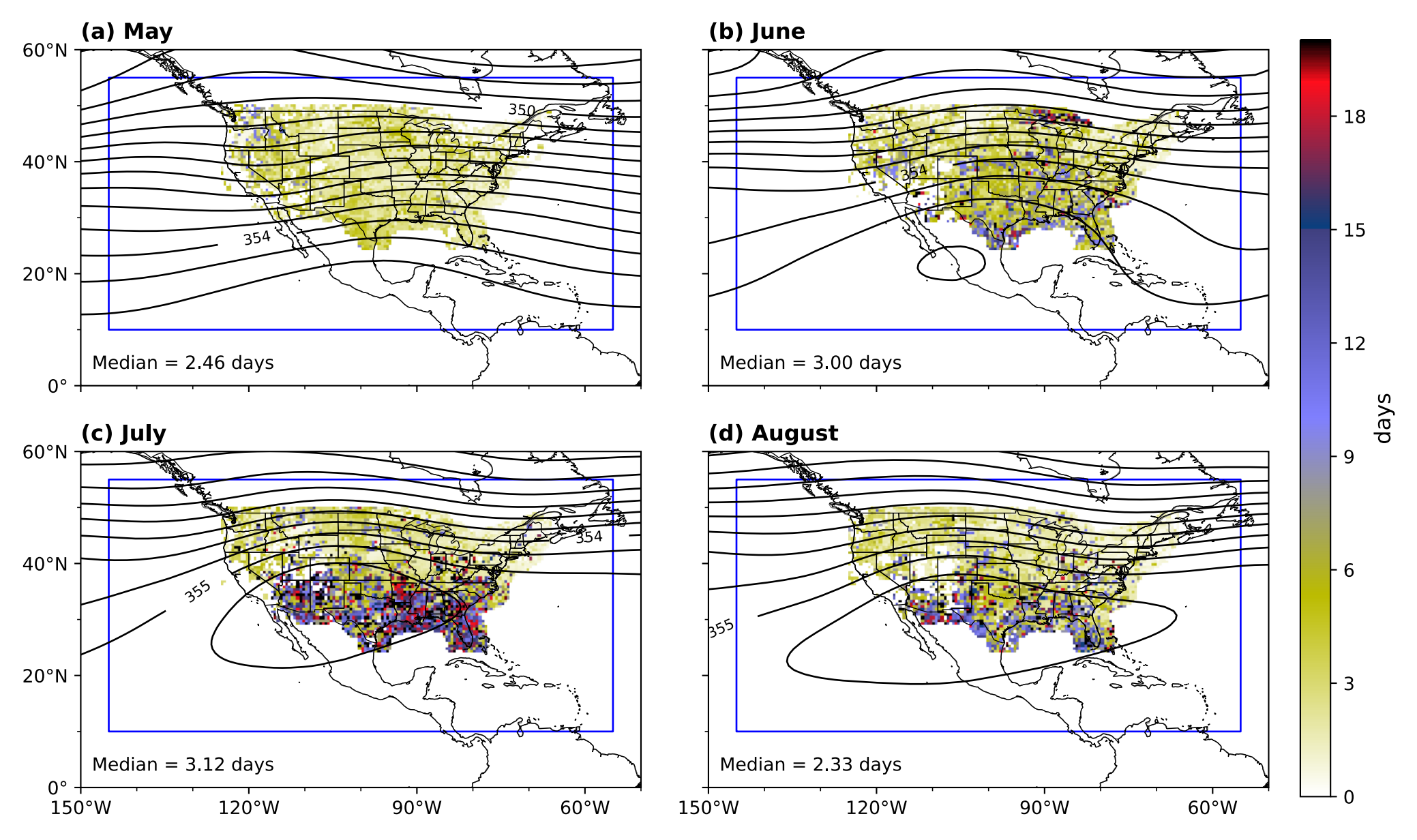
(a) May
(b) June
(c) July
(d) August
60°N
40°N
20°N
0°
150°W
120°W
90°W
60°W
350
354
355
Median = 2.46 days
Median = 3.00 days
Median = 3.12 days
Median = 2.33 days
0
3
6
9
12
15
18
days

Figure 7.

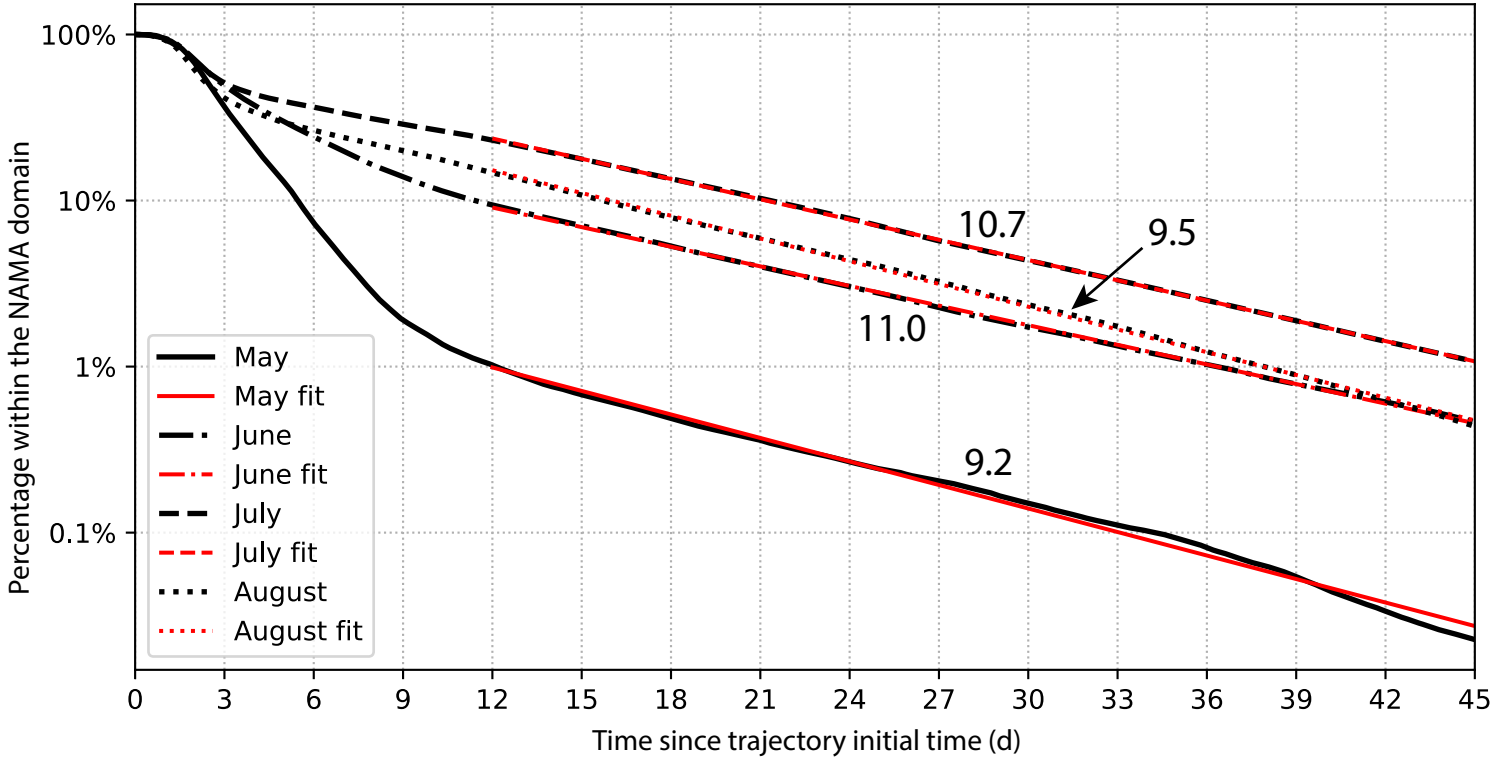
100%
10%
1%
0.1%
Percentage within the NAMA domain
0
3
6
9
12
15
18
21
24
27
30
33
36
39
42
45
Time since trajectory initial time (d)
May
May fit
June
June fit
July
July fit
August
August fit
10.7
9.5
11.0
9.2

Figure 8.

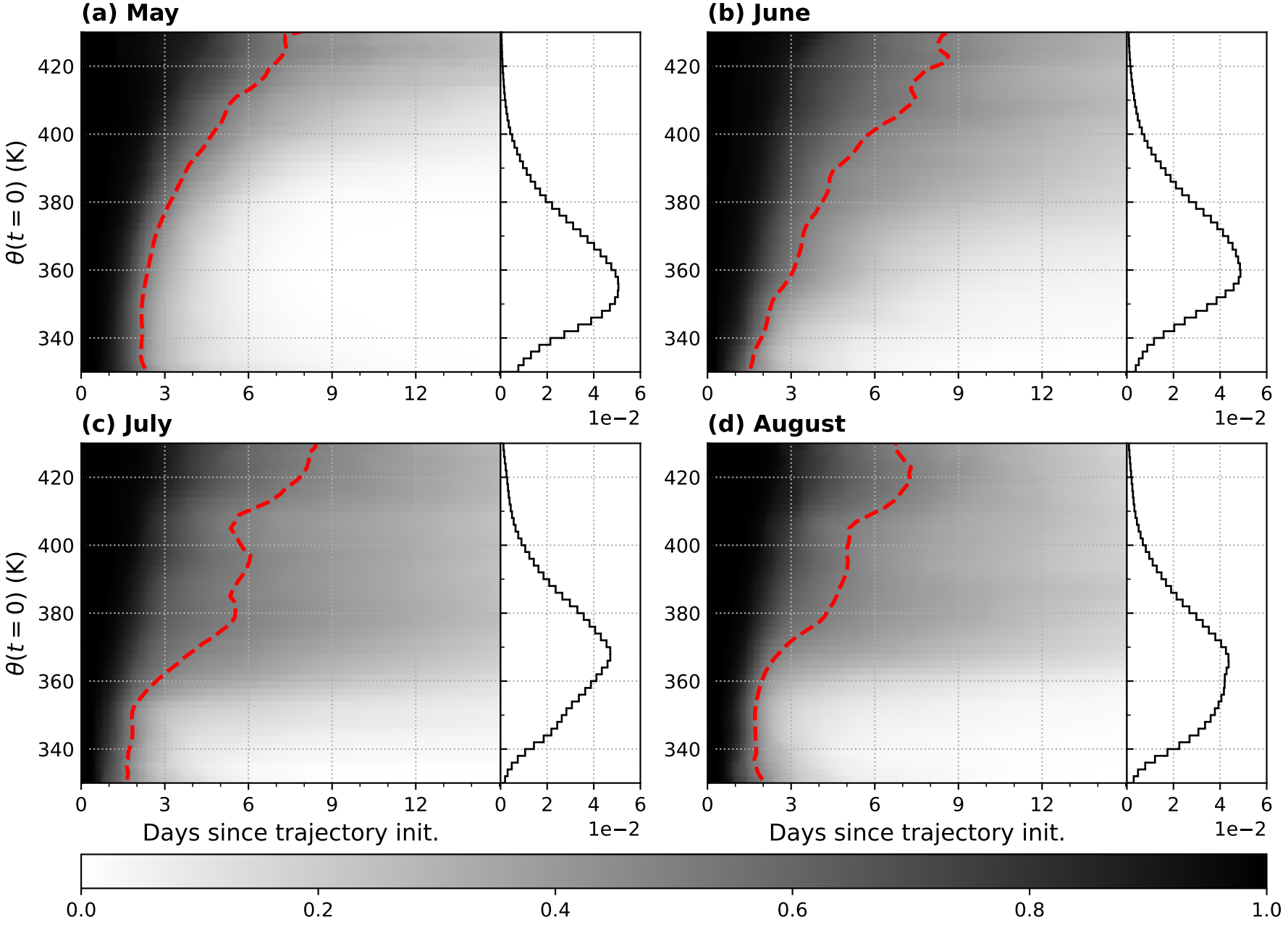
(a) May
(b) June
(c) July
(d) August
θ(t = 0) (K)
420
400
380
360
340
0
3
6
9
12
0
2
4
6
1e−2
Days since trajectory init.
0.0
0.2
0.4
0.6
0.8
1.0

Figure 9.

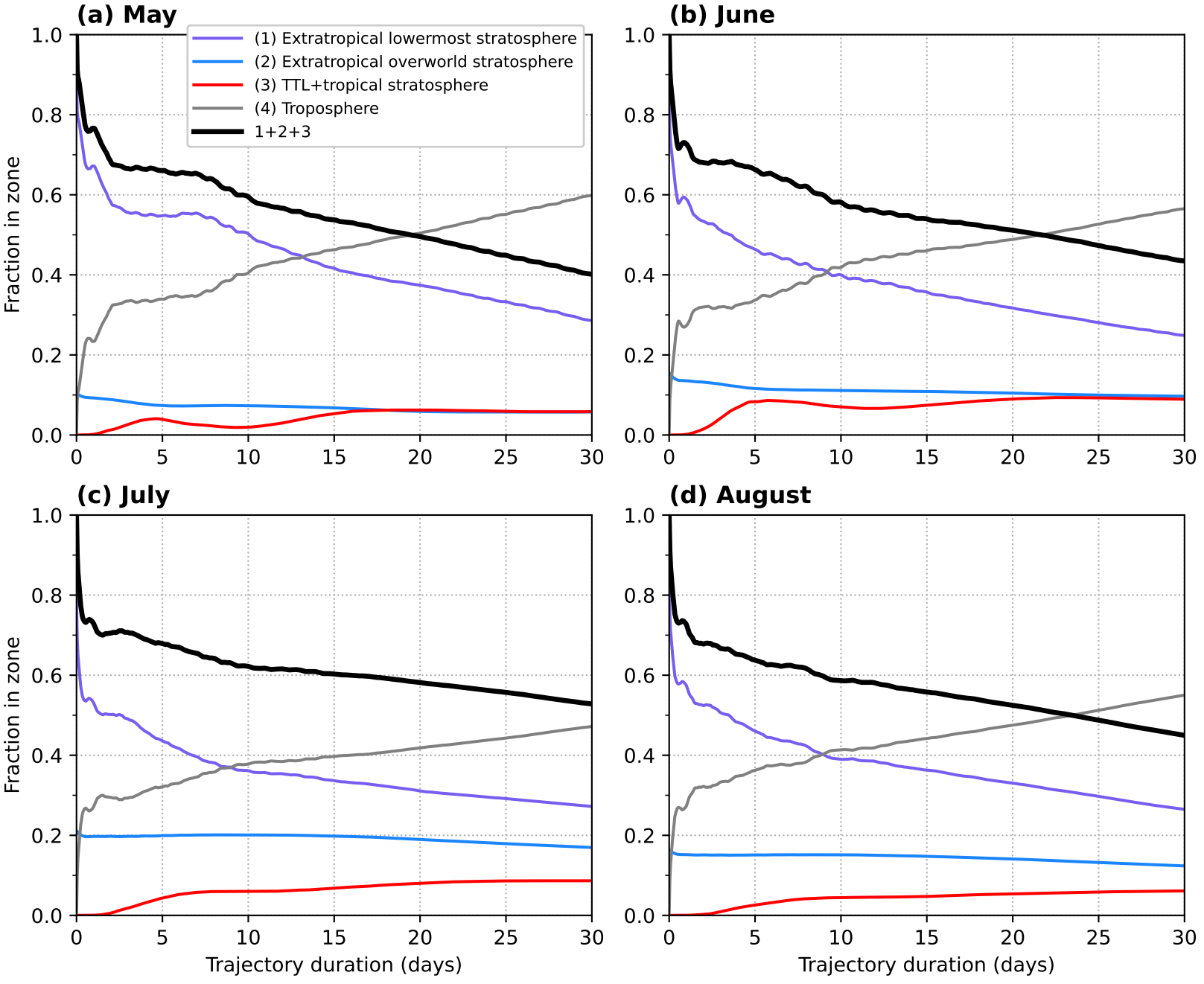
(a) May
(b) June
(c) July
(d) August
(1) Extratropical lowermost stratosphere
(2) Extratropical overworld stratosphere
(3) TTL+tropical stratosphere
(4) Troposphere
1+2+3
Fraction in zone
Trajectory duration (days)
0.0
0.2
0.4
0.6
0.8
1.0
0
5
10
15
20
25
30

Figure 10.

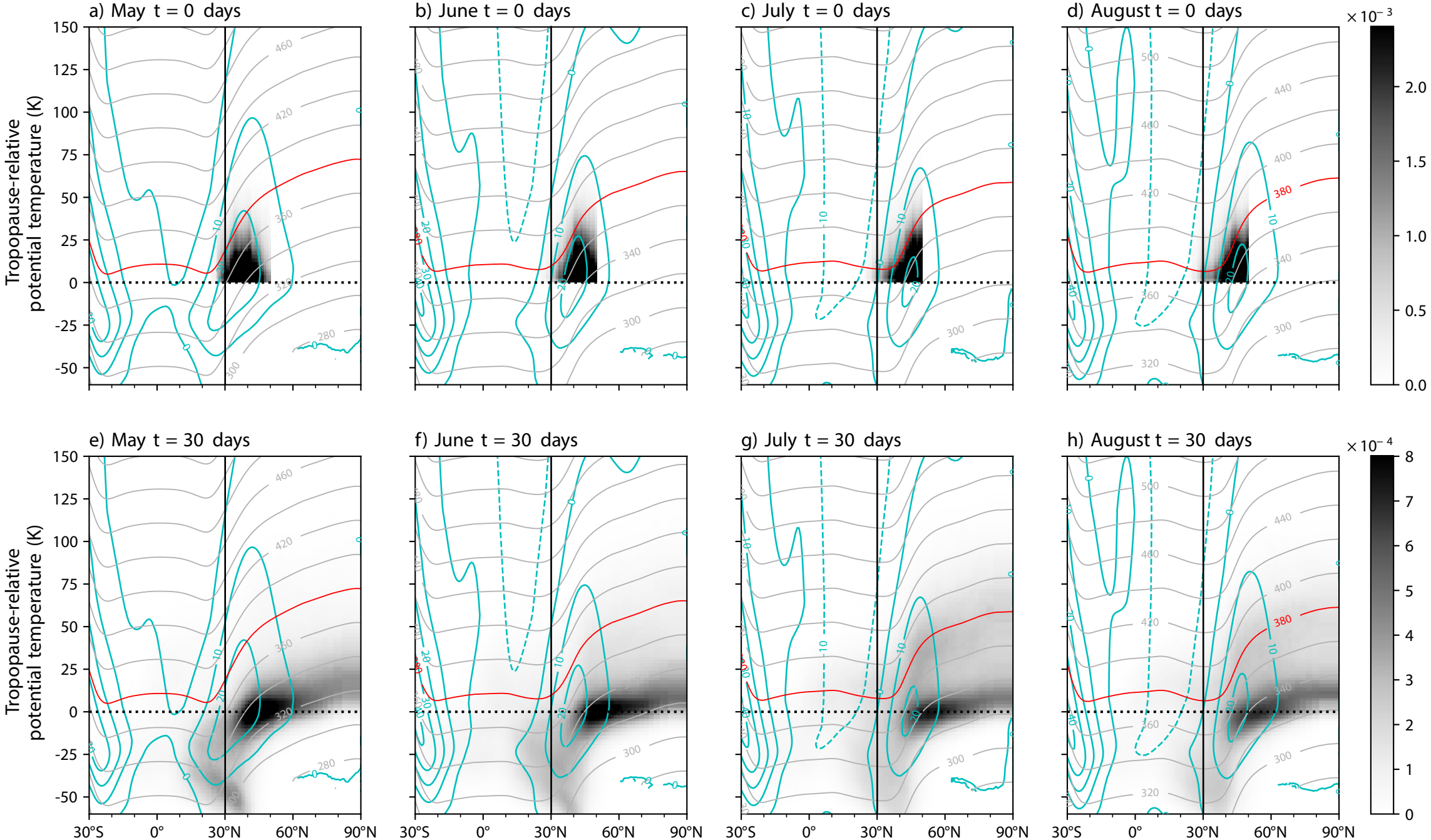
a) May t = 0 days
b) June t = 0 days
c) July t = 0 days
d) August t = 0 days
e) May t = 30 days
f) June t = 30 days
g) July t = 30 days
h) August t = 30 days
Tropopause-relative potential temperature (K)
150
125
100
75
50
25
0
-25
-50
30°S
0°
30°N
60°N
90°N
× 10⁻³
2.0
1.5
1.0
0.5
0.0
× 10⁻⁴
8
7
6
5
4
3
2
1
0

Figure 11.

a) May t = 0 days
b) June t = 0 days
c) July t = 0 days
d) August t = 0 days
e) May t = 30 days
f) June t = 30 days
g) July t = 30 days
h) August t = 30 days
i) May t = 0 days
j) June t = 0 days
k) July t = 0 days
l) August t = 0 days
m) May t = 30 days
n) June t = 30 days
o) July t = 30 days
p) August t = 30 days
Tropopause-relative potential temperature (K)
Jet-relative latitude
$\times 10^{-3}$
$\times 10^{-4}$
6% 26% 32% 34% 20%
8% 23% 31% 33% 22%
11% 28% 39% 25% 19%
7% 24% 31% 20% 18%
15% 34% 49% 33% 14%
18% 33% 51% 33% 14%
21% 40% 61% 24% 12%
18% 40% 58% 22% 13%

Figure 12.

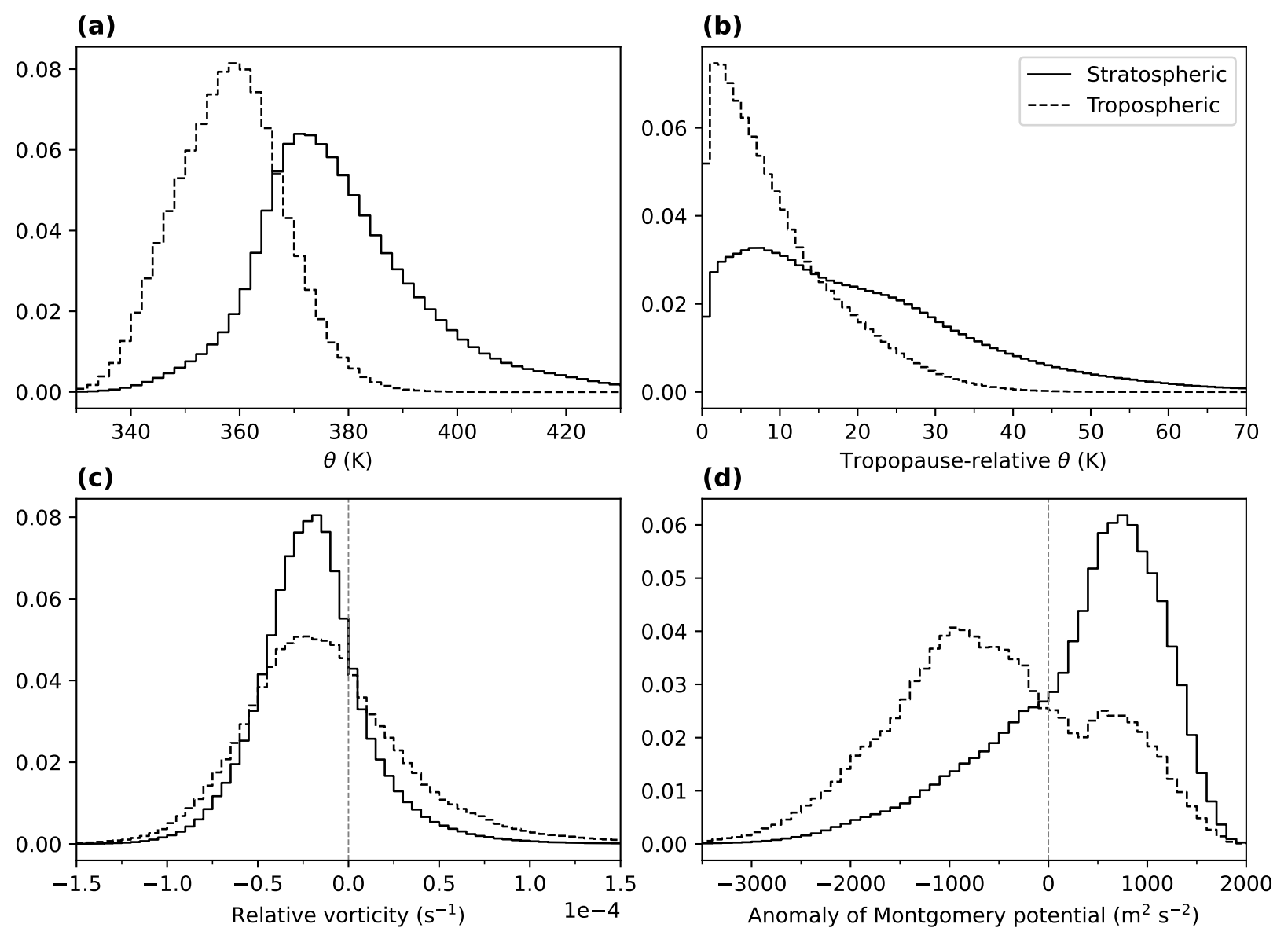
(a)
0.08
0.06
0.04
0.02
0.00
340
360
380
400
420
θ (K)
(b)
Stratospheric
Tropospheric
0.06
0.04
0.02
0.00
0
10
20
30
40
50
60
70
Tropopause-relative θ (K)
(c)
0.08
0.06
0.04
0.02
0.00
−1.5
−1.0
−0.5
0.0
0.5
1.0
1.5
1e−4
Relative vorticity (s^{-1})
(d)
0.06
0.05
0.04
0.03
0.02
0.01
0.00
−3000
−2000
−1000
0
1000
2000
Anomaly of Montgomery potential (m^2 s^{-2})

Figure 13.

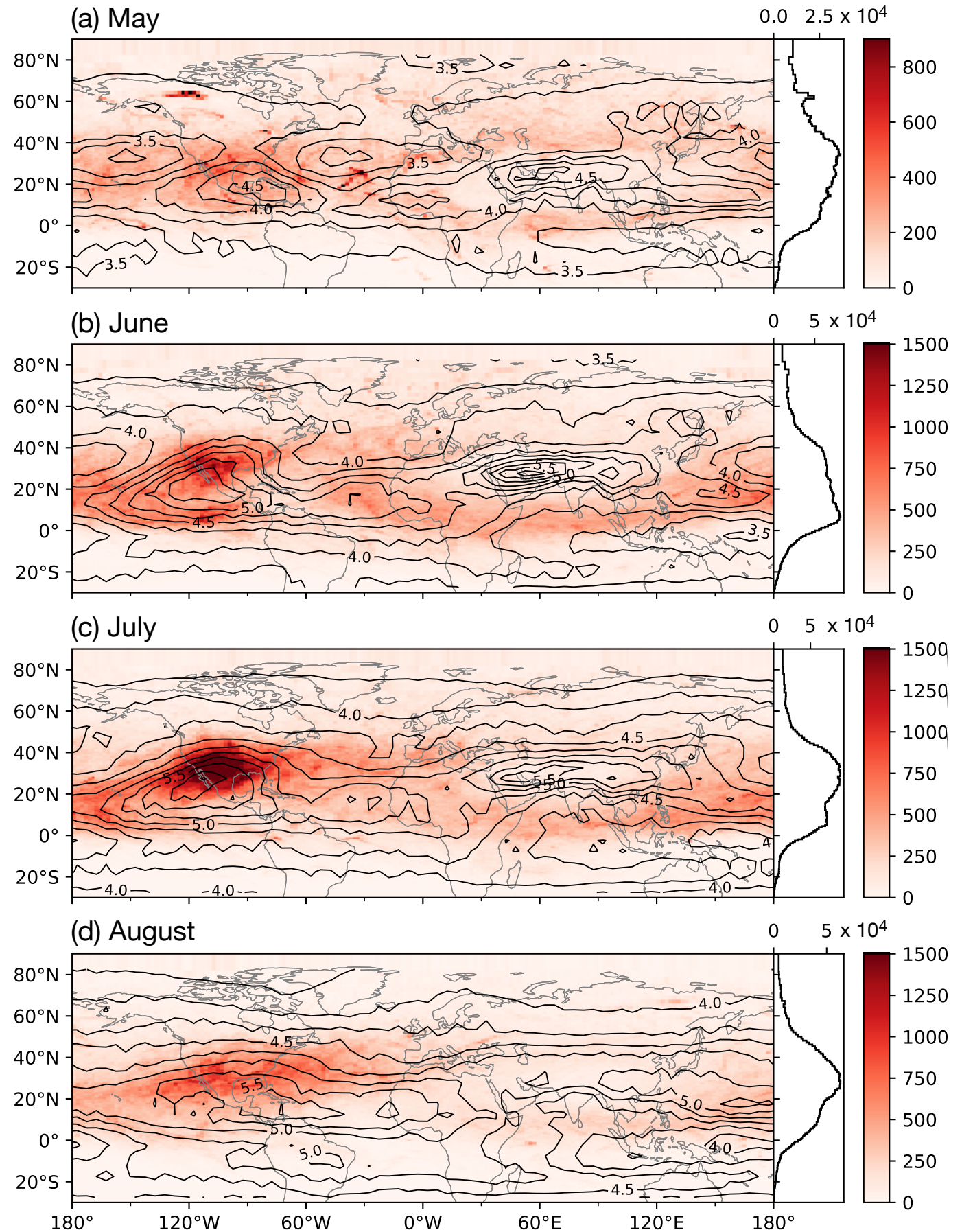
(a) May
0.0 2.5 x 10^4
(b) June
0 5 x 10^4
(c) July
0 5 x 10^4
(d) August
0 5 x 10^4
80°N
60°N
40°N
20°N
0°
20°S
180°
120°W
60°W
0°W
60°E
120°E
180°
3.5
4.0
4.5
5.0
5.5
0
200
400
600
800
250
500
750
1000
1250
1500

Transport and Confinement of Plumes from Tropopause-Overshooting Convection over the Contiguous United States During the Warm Season

Kai-Wei Chang, Kenneth P. Bowman, and Anita D. Rapp

Department of Atmospheric Sciences, Texas A&M University, College Station, Texas

Key Points:

- Three-dimensional diabatic trajectories are used to assess the transport of air masses from tropopause-penetrating convection
- The North American monsoon anticyclone confines air masses over North America and also aids the transport of air into the stratosphere
- About 45% of air injected into the stratosphere by tropopause-overshooting convection remains in the stratosphere after 30 days

Corresponding author: Kai-Wei Chang, kwchang30@tamu.edu

Abstract

Tropopause-penetrating overshooting convection (OC) can transport tropospheric air into and affect the composition of the lower stratosphere. During the warm season, OC occurs frequently over the contiguous United States, and the transport of plumes from these events is modulated by the flow over North America, which throughout June to August is characterized by a large-scale anticyclone in the upper troposphere and lower stratosphere. This study uses data from the Next Generation Weather Radar (NEXRAD) and the ERA5 reanalysis to locate OC during May–August of 2008 to 2020. Evidence of convective transport is found well above the 380 K isentrope, which is the top of the "lowermost stratosphere" and also the top of the stratospheric middleworld. By initializing massless particles within the volume of OC above the tropopause, we perform trajectory calculations to simulate the transport of OC plumes. With three-dimensional diabatic trajectory modeling in isentropic coordinates using winds from ERA5, we quantify the confinement within the anticyclone and the number of trajectories transported into the tropical and extratropical stratosphere. By evaluating the trajectory residence time in the North American region, we find that July exhibits the strongest confinement, with about a quarter of trajectories staying in the region for more than 11 days. It is shown that, together with sufficient injection height, convective injection that occurs south of the jet and/or into anticyclonic regimes increases the chances of air remaining in the stratosphere. After 30 days, 45% of all air masses injected above the tropopause remain in the global stratosphere.

Plain Language Summary

1 Introduction

Cross-tropopause overshooting convection can rapidly transport constituents from the boundary layer into the lowermost stratosphere (LMS) (Fischer et al., 2003) and influence the composition of air in the LMS. There is evidence that deep convection is capable of lofting ice into and hydrating the stratosphere (Hanisco et al., 2007; Nielsen et al., 2007; Corti et al., 2008; de Reus et al., 2009). Stratospheric water vapor influences surface climate (Forster & Shine, 2002; Solomon et al., 2010) and plays a role in stratospheric chemistry (Anderson et al., 2012, 2017). Furthermore, anthropogenic pollutants also reach the stratosphere via convective transport (Randel et al., 2010; Vernier et al., 2015). Deep convection is a potential pathway for very short-lived substances (VSLS)

that could potentially lead to ozone depletion (Hossaini et al., 2015, 2017). As such, improving our understanding of mixing and transport processes associated with overshooting convection is crucial for addressing uncertainties in climate and stratospheric chemistry.

The influence of deep convection on the composition of the upper troposphere and lower stratosphere (UTLS) is evident in the North Hemispheric warm season. In the regions associated with the Asian Monsoon (AM) and North American Monsoon (NAM), air transported into the UTLS tends to be trapped by the anticyclones forced by precipitation from the AM (Li et al., 2005; Park et al., 2007, 2008; Ungermann et al., 2016; Siu & Bowman, 2019; Legras & Bucci, 2020) and the NAM (Li, 2005; Clapp et al., 2019, 2021; Chang et al., 2021). Using hourly observations from the National Oceanic and Atmospheric Administration Next Generation Weather Radar (NEXRAD), Cooney et al. (2018) showed that in each year there are about 45,000 overshooting events over the contiguous United States (CONUS) that exhibit echo-top heights of 1 kilometer or more above the tropopause. Furthermore, approximately 45% of those events reach above the 380 K isentropic level into the overworld stratosphere. Given that deep overshooting events occur frequently over the CONUS, air in the North American Monsoon Anticyclone (NAMA) is expected to be significantly influenced by convection. For instance, deep convection over the U.S. has been shown to moisten the UTLS over North America (Poulida et al., 1996; Dessler & Sherwood, 2004; Hanisco et al., 2007; Anderson et al., 2012; Schwartz et al., 2013; Herman et al., 2017; Smith et al., 2017; Jensen et al., 2020; Werner et al., 2020; Yu et al., 2020; Tinney & Homeyer, 2021). Aside from vertical transport of moisture by convection, isentropic mixing also is important for the transport of moisture between the tropical upper troposphere and extratropical lower stratosphere (Dethof et al., 2000). Though many studies suggest that deep overshooting events can hydrate the stratosphere, it is not well understood how air from overshooting convection over the CONUS is transported by the large-scale flow.

Compared to the transport due to the circulation associated with the AM, the UTLS transport in the NAM region is less studied. Yan et al. (2019) showed that, despite the AM having a larger contribution to the mass transport into the stratosphere, both regions have similar efficiencies in mixing air mass into the tropical pipe. Clapp et al. (2019) studied the effects of NAMA on convectively influenced air mass (CIAM) and identified source regions of CIAM identified using the Geostationary Operational Environmental

Satellite (GOES) imagery. They found that the NAMA has the strongest influence on CIAMs in August. In a related study, Clapp et al. (2021) showed that the NAMA influences the meridional transport of CIAMs, particularly in July and August, during when CIAMs are on average transported 22° northward. However, as both of these studies were based on data from a single year (2013), interannual variability may affect their findings.

In this study, we utilize NEXRAD observations and the ERA5 reanalysis from 2008 to 2020 to investigate how CIAMs originating from convection over the CONUS are transported during the warm season (May–August). We focus on evaluating the degree of confinement due to the UTLS anticyclonic flow, and also on the number of CIAMs that are irreversibly transported into the stratosphere. NEXRAD data and the lapse-rate tropopause derived from ERA5 are used to detect overshooting convection, and diabatic trajectory calculations (using diabatic heating rate as vertical motion) are deployed to assess how CIAMs are transported after they have been injected into the stratosphere.

2 Data and Methods

2.1 GridRad

GridRad (Bowman & Homeyer, 2017) is a gridded radar data set based on radar reflectivity from NEXRAD WSR-88D radar observations. The GridRad algorithm merges NEXRAD data from 143 sites throughout the CONUS into a three-dimensional, regularly gridded (approximately 0.02° × 0.02° × 1 km) data set with 1-hour temporal resolution. We use GridRad version 4.2 data to identify hydrometeors above the tropopause during May through August of 2008 to 2020.

2.2 ERA5 reanalysis

ERA5 (Hersbach et al., 2020) is the fifth-generation reanalysis from ECMWF and is based on the Integrated Forecast System (IFS) Cy41r2. The native resolution of the IFS is TL639 (31 km) and 137 hybrid sigma-pressure levels. In this study, ERA5 is used for tropopause altitude and trajectory calculations. The resolution of the ERA5 data used in this study is 0.75°× 0.75°. Temperature from the hourly pressure-level data with 37 unevenly-spaced vertical levels are used to calculate the WMO definition of the lapse-rate tropopause (WMO, 1957), defined as the lowest altitude at which the lapse rate de-

creases to 2 K km^{-1} or less and the average lapse rate between this altitude and all higher altitudes within 2 km does not exceed 2 2 K km^{-1}

For trajectory calculations, zonal and meridional winds are obtained from the isentropic-coordinate ERA5 data. Diabatic heating rates are provided by the "mean temperature tendency due to parameterizations" variable in the ERA5 model-level data. This variable is the sum of the parameterized temperature tendencies due to shortwave/longwave radiation, latent heating, sensible heating, and diffusion. We calculate the vertical velocity in isentropic coordinates, $d\theta/dt$, using

$$c_p \frac{d\theta}{dt} = Q \frac{\theta}{T} \tag{1}$$

where c_p is the specific heat at constant pressure, θ is potential temperature, Q is the temperature tendency, and T is temperature. Horizontal winds are taken from 1-hourly isentropic-level data, while heating rates are from 3-hourly model-level data.

2.3 Lagrangian forward trajectories

The TRAJ3D trajectory model (Bowman, 1993) is used in this study to characterize the three-dimensional Lagrangian motion of convectively-influenced air parcels. TRAJ3D uses a standard fourth-order Runge-Kutta scheme to solve the kinematic equations of motion

$$\frac{d\mathbf{x}(t)}{dt} = \mathbf{v}[\mathbf{x}(t)] \tag{2}$$

where $\mathbf{x}(t)$ is the particle position at time t and $\mathbf{v}[\mathbf{x}(t)]$ is the particle velocity at position $\mathbf{x}$ and time t. Trajectories are calculated in isentropic coordinates with a time step of 15 minutes. Zonal and meridional winds are taken from the hourly isentropic-level ERA5 data. The potential temperature (θ) levels used are 320, 330, 350, 370, 395, 430, and 475 K. Vertical velocities $d\theta/dt$ are first calculated on the ERA5 sigma-pressure levels using the temperature tendency, and then interpolated to the θ levels. Particles that descend below 320 K are considered out of bounds and are no longer tracked. The lower bound of 320 K is enforced because this θ surface may intersect the earth's material surface, especially in the tropics.

2.4 Overshooting top identification and trajectory spawning

The vertical extent of hydrometeors is determined using the radar echo top height z_e, which we define as the maximum height with a valid radar reflectivity of at least 10

dBZ. The threshold of 10 dBZ is determined based on tests performed by Cooney et al. (2018) who found that this threshold provides the best balance between sensitivity and noise for the detection of overshooting tops. To find the echo-top pressure, $p_e = p(z_e)$, geopotential height from the pressure-level ERA5 data is horizontally interpolated to the GridRad grid and then p_e is obtained by vertical interpolation.

The WMO tropopause pressure and height, p_t and z_t, are first calculated on the ERA5 grid ($0.75° \times 0.75°$) and then horizontally interpolated to the GridRad grid. Wherever there is a valid value of z_e, the overshoot extent is evaluated as $z_e - z_t$. Echo tops that satisfy $z_e - z_t \geq 1$ km are identified as overshooting tops. Cooney et al. (2018) performed a quality control analysis to assess the validity of GridRad-detected overshoots by manually inspecting reflectivity profiles and soundings of roughly 13,000 overshoot cases. They find that there is a higher chance of detected overshoots to be spurious if the echo-top height satisfies either of the following conditions:

$$z_e > 10 + 0.33(dBZ_{\max} - 20), \text{ or} \tag{3}$$

$$z_e - z_t > 1 + 0.154(dBZ_{\max} - 15) \tag{4}$$

where z_e and z_t are the echo-top and tropopause height in kilometers, and $dBZ_{\max}$ is the column maximum reflectivity. We exclude any overshoots that satisfy either condition from our analysis. Out of 8,360,388 overshooting GridRad pixels in the analysis period that are +1 km above the tropopause, 1,363,287 are excluded by using these criteria.

Trajectories are initialized using p_e, p_t, and the longitude and latitude of the GridRad grid boxes, and are run forward for 45 days. At a GridRad grid box centered on longitude x and latitude y where an valid overshooting top is detected ($z_e - z_t \geq 1$ km is satisfied), a trajectory is initiated at the midpoint of every 1 hPa layer between p_e and p_t. As an example, if $p_e = 144.5$ hPa and $p_t = 140.5$ hPa then $\lceil p_e \rceil = 145$ and $\lfloor p_t \rfloor = 140$ and trajectories are initiated at pressures 140.5, 141.5, 142.5, 143.5, and 144.5 hPa. These pressure values are converted to potential temperature in order to run the trajectory on isentropic coordinates. Trajectories are initiated evenly in pressure coordinates because the resulting number of trajectories will be proportional to the mass that is influenced by overshooting convection. The longitude and latitude of the trajectories' initial positions are specified as the center of the grid box x and y, and the initial time is taken as the time of the hourly GridRad analysis.

3 Results

3.1 Climatology of winds

Figures 1 and 2 show monthly climatologies of Montgomery streamfunction and $d\theta/dt$ at isentropic levels 400, 360, and 350 K for 2008–2020. During May, the flow over the U.S. and northern Mexico is characterized by westerlies, with the time-averaged anticyclone located to the south. In June, the NAMA is present at 400 and 360 K and its influence is mainly over Mexico and the U. S. southern border. In July and August the NAMA is located somewhat farther north, with a climatological anticyclone present at all three altitudes. While the NAMA at 400 and 360 K is characterized by positive diabatic heating, that is not the case at 350 K, where the NAMA exhibits mostly diabatic cooling except in the regions associated with the North American monsoonal precipitation along the west coast of Mexico. During June–August, the southwestern portions of anticyclones at 360 and 400 K exhibit positive heating characteristics while the eastern edges of the NAMA exhibits weaker heating (or even cooling). This suggests that air mass injected into the interior of the anticyclone is likely to be transported upward due to the positive diabatic heating.

Vertical cross-sections of mean zonal wind and diabatic heating within 145°–55°W for May, June, July and August are shown in Figure 3. Within about 30° of the equator, the positive diabatic heating associated with the tropical tropopause layer and tropical stratosphere is present at potential temperatures of roughly 360 K and above. At around 10°N and below 350 K there is strong positive heating associated with convection from the inter-tropical convergence zone as well as convection near Panama and Colombia. Poleward of 30°N, there is cooling throughout the column, with stronger cooling present between 340 and 360 K, indicating subsidence at higher latitudes.

3.2 Confinement of convectively influenced air mass

The total number of trajectories spawned in each month is shown in Table 1. The total number of trajectories, which is roughly proportional to the mass of convectively influenced air (since they are initialized evenly in pressure), is highest in June, followed by May, July, and August. This is also consistent with the frequency of overshoots reaching 1 km or more above the local tropopause shown in Cooney et al. (2018) (cf. their Figure 6). The spatial patterns of trajectory counts, shown in the left column of Figure

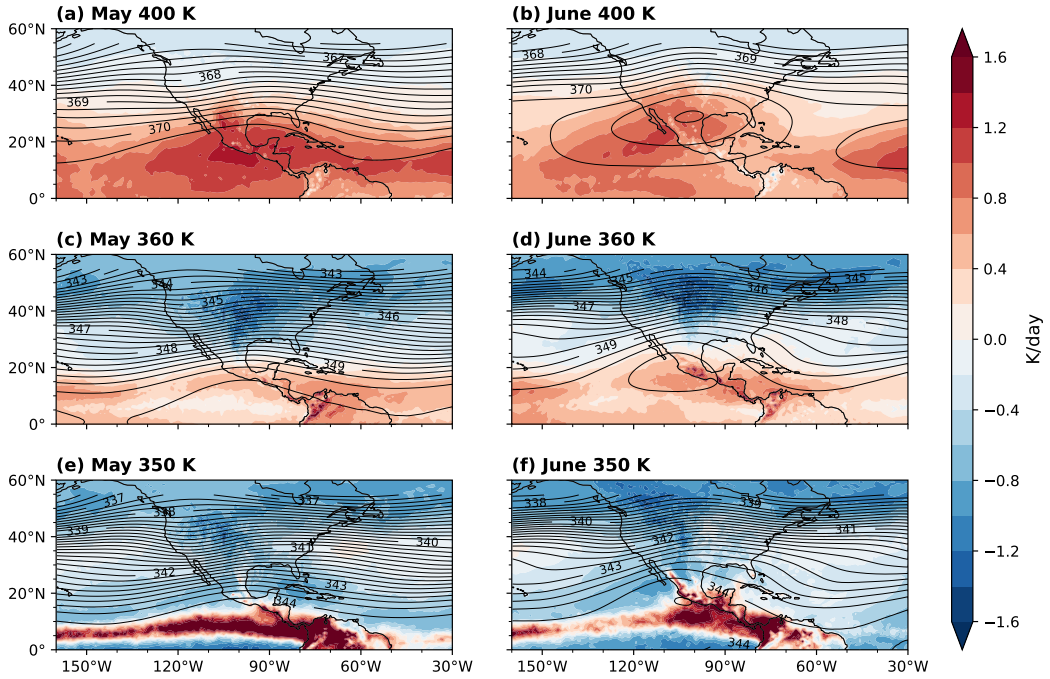

Figure 1. Climatology of 2008–2020 ERA5 $d\theta/dt$ (filled contours) and Montgomery streamfunction (black) for May (a, c, e) and June (b, d, f). Panels a–b show values for the 400 K isentropic level level, while c–d and e–f are for 360 K and 350 K, respectively. Filled (black) contours have intervals of 0.1 K d^{-1} (0.25 kJ kg^{-1}).

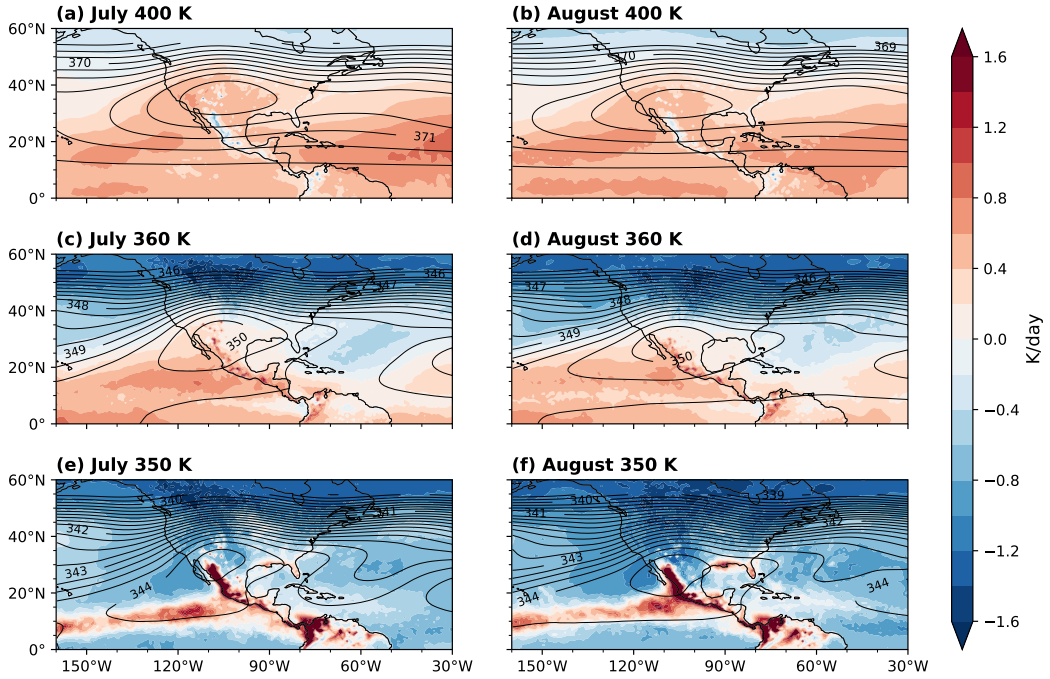

Figure 2. Same as Figure 1 except for July (a, c, e) and August (b, d, f).

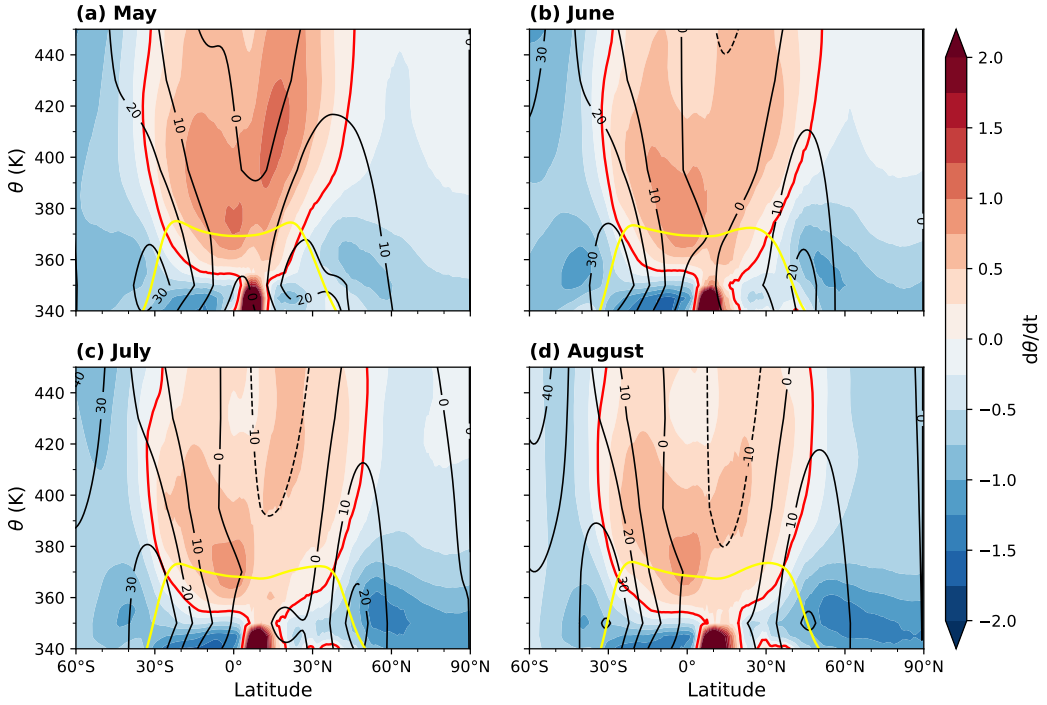

Figure 3. Zonal-mean $d\theta/dt$ (filled) and zonal wind (black) within 145°–55°W for (a) May, (b) June, (c) July, and (d) August. Filled (black) contours have intervals of 0.25 K day^{-1} (10 m s^{-1}). Thick red line denotes the zero contours of $d\theta/dt$ and yellow lines indicate the mean tropopause.

	May		June		July		August	
Total	48.8		66.1		44.8		35.3	
τ_r >5.5 d	4.7	(9.7%)	18.4	(27.8%)	16.9	(37.6%)	9.3	(26.4%)

Table 1. Total number of trajectories ($\times 10^6$) spawned in each month and the number of trajectories with τ_r greater than 5.5 d, which is the 75% percentile of τ_r for the entire season. Percentages in parenthesis are fraction in each month that exceed 5.5 d.

	May	June	July	August	All months
Mean	3.1	5.2	7.8	5.8	5.4
25th percentile	1.7	1.8	1.8	1.5	1.7
50th percentile	2.4	2.9	3.0	2.4	2.7
75th percentile	3.6	5.8	11.0	6.2	5.5

Table 2. Mean τ_r within the NAMA domain and selected percentiles of the τ_r distributions. Units are days.

4, resemble the frequency of overshooting convection shown by Cooney et al. (2018) (cf. their Figure 10).

To assess the degree of confinement the NAMA has on CIAMs, we use the blue box in Figure 4 to evaluate the residence time τ_r in the NAMA region. We define τ_r as the interval between the initial trajectory time and the first time that the trajectory exits the domain. Horizontally, the domain is defined as 145°W–55°W, 10°N–55°N, and vertically the base is at 320 K. This domain is considerably larger than the size of the climatological NAMA because the position and size of the NAMA exhibits intraseasonal synoptic-scale variability.

Figure 5 shows the probability density function (PDF) as well as the cumulative distribution function (CDF) of τ_r, while Table 2 shows the mean τ_r and the 25^{th}, 50^{th}, 75^{th} percentiles. The differences between the monthly PDFs, which are positively skewed, are greatest in the tails of the distributions. The 25^{th} and 50^{th} percentile values are similar among the months, while the 75^{th} percentile for July (11 d) is significantly higher than June and August (∼6 d), and May (3.6 d) is significantly lower.

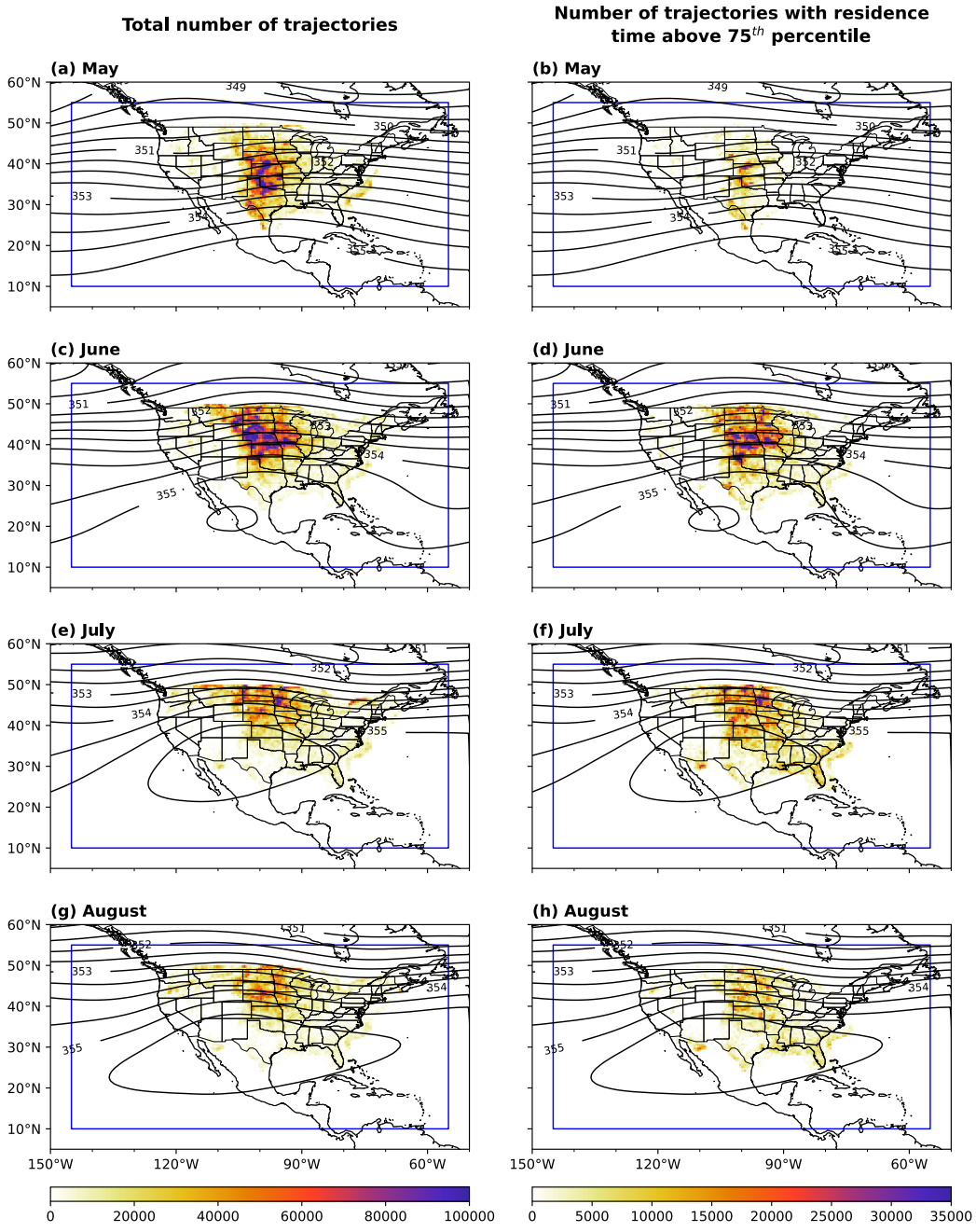

Figure 4. Total number of trajectories initiated in each 0.5° × 0.5° bin for each month (left column) and the number of trajectories with τ_r longer than 5.5 d, which is 75th percentile of the overall distribution (right column; see Table 2). Black contours represent the 2008–2020 monthly mean 370 K Montgomery streamfunction at intervals of 0.5 kJ kg^{-1}. The blue box delineates the domain used to calculate τ_r of trajectories in the NAMA domain.

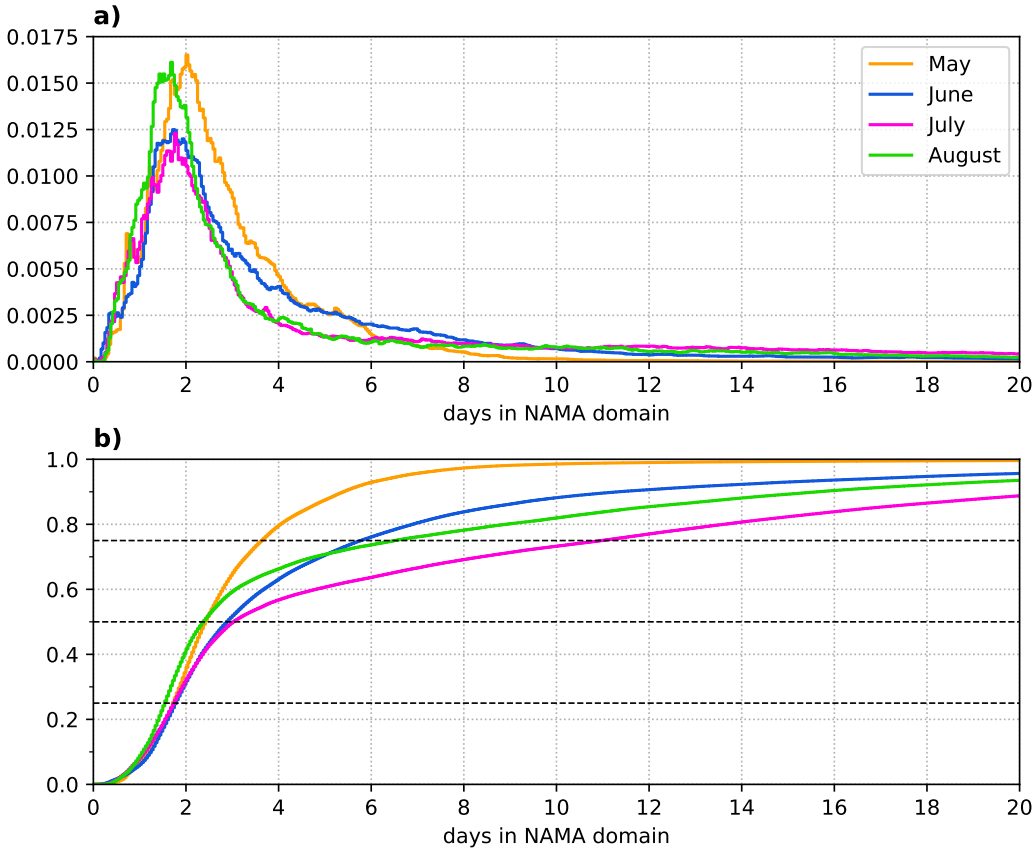

Figure 5. (a) Normalized density functions of τ_r in the NAMA domain for particles spawned in May (orange), June (blue), July (magenta), and August (green) in 2008–2020. (b) Cumulative distribution function of τ_r. Dashed lines indicate the 25^{th}, 50^{th}, 75^{th} percentiles.

The 75$^{\text{th}}$ percentile for all months combined is 5.5 days. Figures 4b, d, f, and h show the number of trajectories from each month whose τ_r is greater than 5.5 days, and Table 1 denotes the number and percentage of trajectories above this τ_r threshold. Though July has the highest percentage of trajectories satisfying this threshold, June has the greater number of trajectories; this demonstrates that the confinement effect is stronger in July, but there are more CIAMs being confined in the NAMA domain during June. Overall there are much more CIAMs with long τ_r values from June and July than from May or August.

The median τ_r for trajectories spawned in each $0.5^\circ \times 0.5^\circ$ bin is presented in Figure 6. During July and August regions with larger median τ_r are generally at lower latitudes, where they fall inside closed streamfunction contours of the time-mean circulation. Though June also has a closed contour, its position is south of the U.S., and the correlation between the NAMA and the spatial pattern of the median distribution is more subtle. Part of the discrepancy between the locations with longer τ_r and the closed contour is that during late June the anticyclone is larger and displaced northward relative to the monthly-mean anticyclone (not shown). The cluster of long τ_r near the U.S–Canada border in June occured during 2018 when particles originating from 29 June were advected into the anticyclone, which was centered over the Eastern U.S. during 29-30 June. During May, the median duration is uniformly low across the CONUS, indicating that most of the CIAMs exit the domain rapidly via eastward advection by the jet. The spatial distributions of median τ_r clearly depict the confinement caused by the anticyclonic flow. As seen in Figure 4, however, there are fewer overshooting events in the southern U.S. during the months when the NAMA circulation is strong, as overshooting shifts northward to where the tropopause is lower and the jet is stronger during those months.

Figure 7 shows the fraction of trajectories that remain in the NAMA domain as a function of trajectory duration. During day 1 the values are nearly flat, while during day 2 there is a rapid decrease. This can be attributed to the fact that most overshoot material is injected near the center of the domain and requires some time to be advected to the eastern edge (assuming predominantly westerly winds). At 370 K, the climatological mean zonal wind values near 40°N, 100°W are 18.3, 17.6, 12.0, and 14.8 m s^{-1} for May, June, July, and August, respectively, and based on these wind speeds the time it takes for material to be advected from the center to the eastern edge of the domain (45° separation and assuming a distance of 85 km per degree) are 2.4, 2.5, 3.7, and 3.0

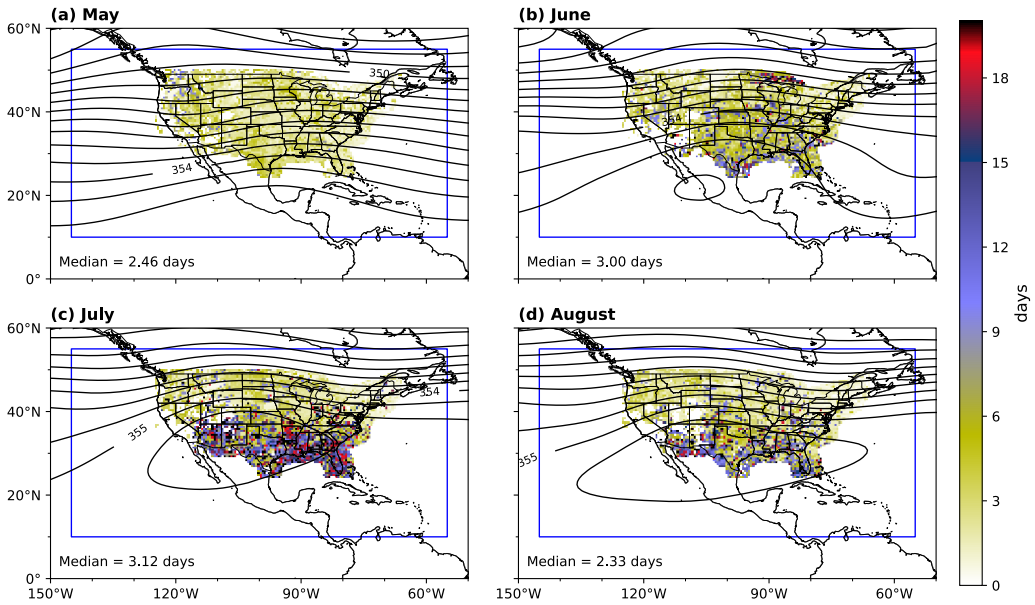

Figure 6. Median τ_r for trajectories by month. The median of all trajectories are denoted in the legend. Black contours represent the monthly mean 370 K Montgomery streamfunction at intervals of 0.5 kJ kg^{-1}.

d for each month. Therefore, during the first day there is little loss of particles. Material injected into the jet reaches the boundary after about a day and then rapidly exits the domain, causing the rapid drop on day 2. After the initial rapid decrease, the slower loss is due to particles partially confined within the NAMA. The linear behavior on this logarithmic plot is consistent with the behavior of steady flow through a well-mixed box with no new sources of particles. In May there is an intermediate period from days 3 to 12 during which the exponential loss rate is faster than what occurs after day 12. In June, July, and August this transition from rapid advective loss to slower well-mixed loss occurs over only a few days. The exponential loss time scales for all four months are about 10 d (see Figure 7 for values), although the initial fractions at the start of the exponential decay are quite different.

Figure 8 shows the PDFs of τ_r as a function of initial trajectory altitude (potential temperature at initial time $\theta(t_0)$). In general, populations with higher initial altitudes tend to have a higher fraction of particles remaining inside the domain for a given time, which is consistent with wind speeds decreasing with altitude above the tropopause. The red lines denote the days at which the fraction reduces to 50% and was calculated

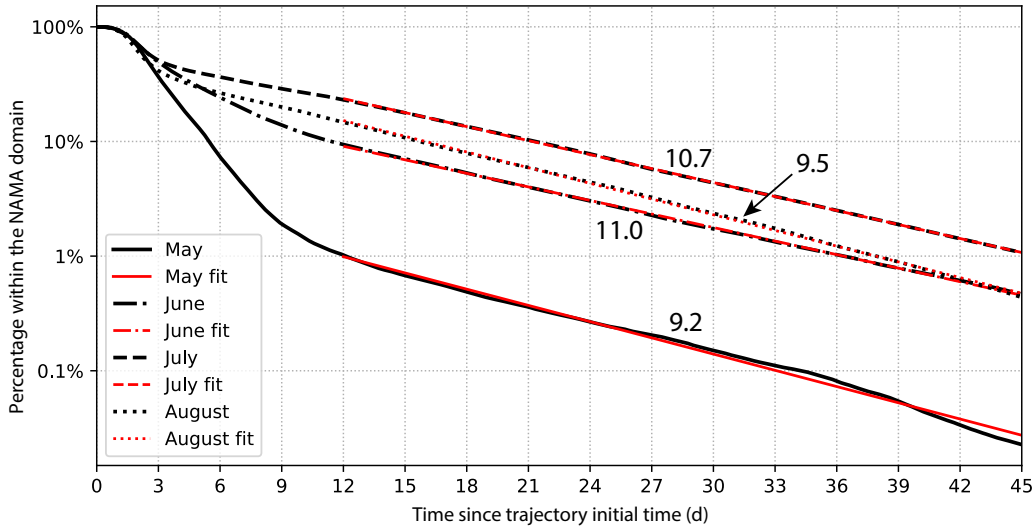

Figure 7. Fraction of the trajectories that has not left the NAMA domain, as a function of trajectory duration. Red lines show the least squares fit to each curve from days 12 to 45. Numerical values are the e-folding time in days estimated from the fits.

by interpolating the fraction at each height. In July and August for trajectories initialized below 360 K, the fraction inside the NAMA domain drops rapidly, while above 360 K the loss of particles is significantly slower.

3.3 Large-scale transport of convectively influenced air

Yu et al. (2020) showed that deep convection over the CONUS moistens the lower stratosphere over North America. The large-scale transport of air mass from this region could potentially spread moisture-rich air over the Northern Hemispheric lower stratosphere and into the tropics. In this section we examine the global transport of CIAMs due to the large-scale circulation.

Because overshooting convection injects trace gases of tropospheric origin into the stratosphere, it is of special interest to understand the number of these plumes staying in the stratosphere after injection. Figure 9 shows the fraction of trajectories in four regions over time: (1) the extratropical lowermost stratosphere (ExLMS, purple); (2) the extratropical overworld stratosphere (blue); and (3) the tropical tropopause layer (TTL) and tropical lower stratosphere (red); and (4) the troposphere (gray). The heavy black line is the total fraction still in the stratosphere. The definitions of the regions used to

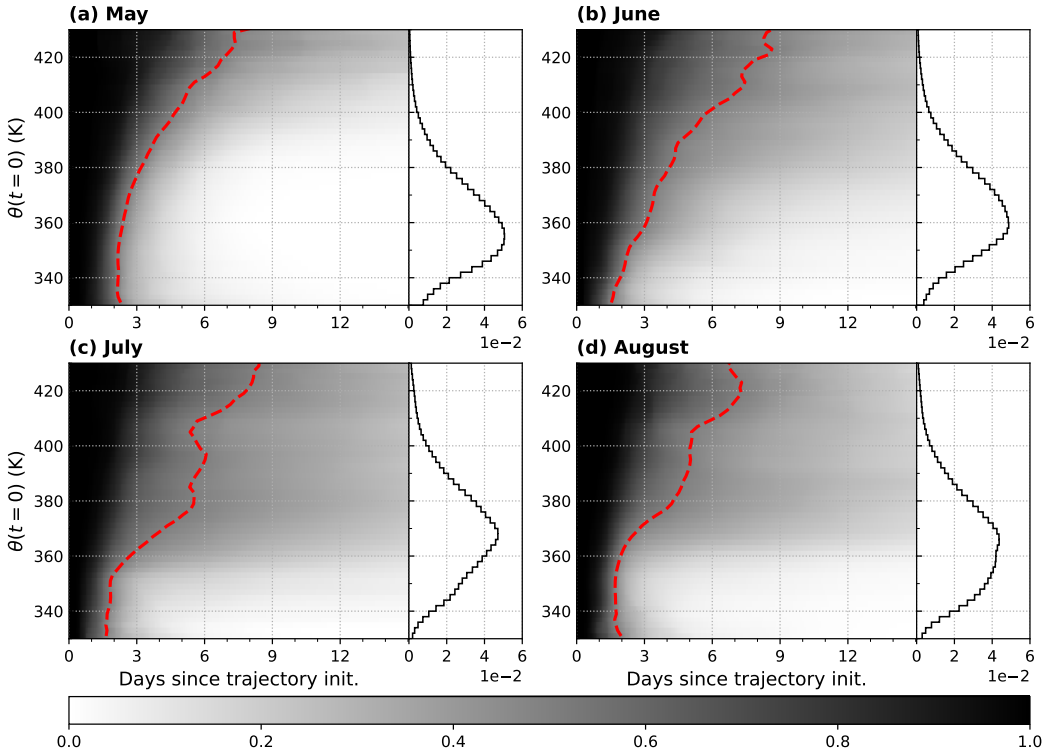

Figure 8. Fraction of particles within 145°W–55°W, 10°N–55°N as a function of time relative to the trajectory initialization, for trajectories initialized in (a) May, (b) June, (c) July, and (d) August. The red dashed line denotes the position of the 0.5 value. The right panels of each plot show the normalized density of the initial potential temperatures $\theta(t = 0)$ of all trajectories initialized in each respective month.

Region	May	June	July	August	All months
Extratropical lowermost stratosphere	28.6	24.9	27.2	26.5	26.6
Extratropical overworld stratosphere	5.8	9.7	17.0	12.4	10.9
TTL + tropical stratosphere	5.8	8.9	8.6	6.1	7.6
Troposphere	59.8	56.5	47.2	55.0	54.9

Table 3. Percentage of trajectories in each region 30 days after being spawned. Region definitions are given in the caption of Figure 9.

categorize the trajectories are given in the figure caption. In all months, an initial rapid loss of particles into the troposphere is observed; amounting to ∼30% over the first 2 to 3 d. After that, there is a slow decrease of the total fraction of trajectories in the stratosphere, consistent with the downward Brewer-Dobson (B-D) circulation in the extratropics. The majority of particles in the stratosphere are in the ExLMS, followed by the extratropical overworld stratosphere. Over time there is a slow increase of trajectories going into the TTL and tropical stratosphere, suggesting that some air plumes originating from overshooting convection over the CONUS are transported into the tropics and end up in the tropical lower stratosphere. This air is likely to ascend in the upward branch of the B-D circulation. Table 3 gives the percentage of trajectories in each stratospheric region after 30 days of transport. In all four months, more than 40% of trajectories are still in the stratosphere after 30 days, with May having the smallest percentage (40%) and July the largest (53%). June and July have a relatively higher percentage of trajectories in the TTL and tropical stratosphere (9% in both months), while July and August have higher percentages in the extratropical overworld stratosphere (17% and 12%, respectively). Overall we find that a significant percentage of air plumes originating from CONUS overshooting convection remain in the global lower stratosphere (45% after 30 days).

In addition to evaluating the fraction of trajectories in stratospheric regions, we also examine the latitude-height cross sections of trajectory distributions to understand transport characteristics. The cross-sections of normalized distributions of the initial ($t = 0$) trajectory locations (Figures 10a–d) show the northward migration of overshoots as the warm seasons progresses from May to August. Overshoot detection by NEXRAD

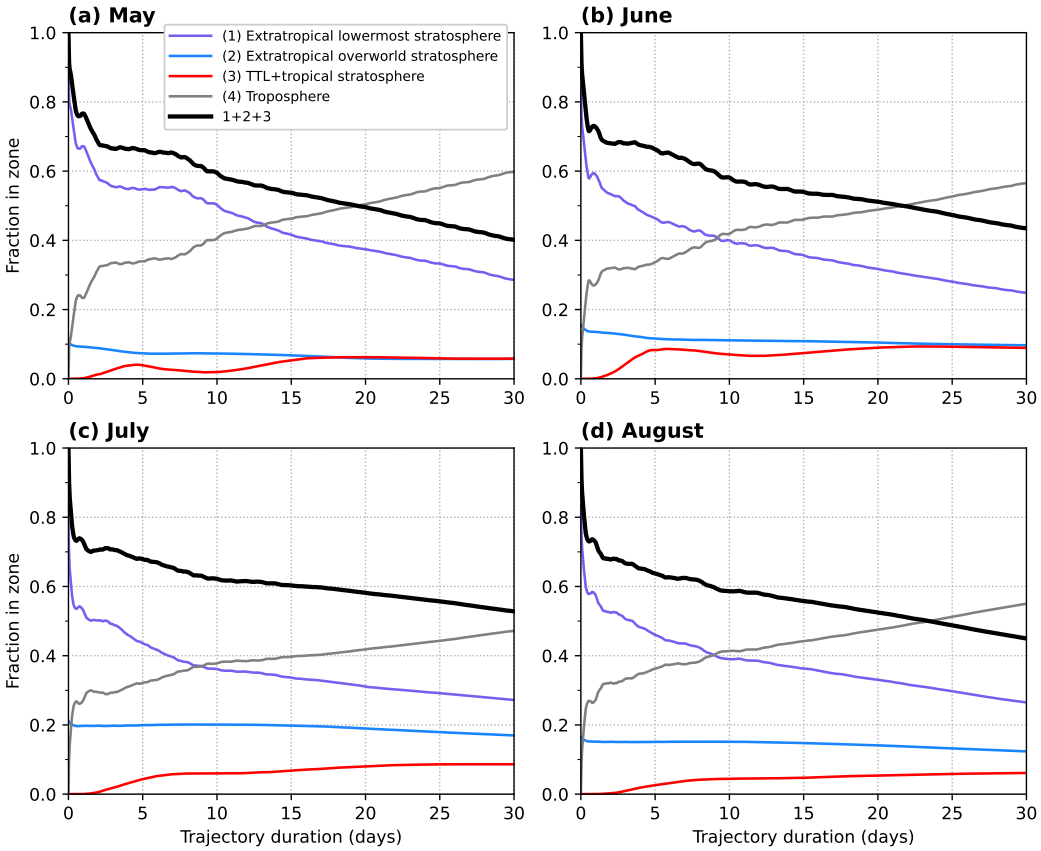

Figure 9. Fraction of particles in various zones over time for trajectories spawned in (a) May, (b) June, (c), July, and (d) August. The zone definitions are: extratropical lowermost stratosphere: $380 \geq \theta > \theta_{trop}$ and $|\phi| > 20°$ where θ_{trop} is the tropopause potential temperature; extratropical overworld stratosphere: $\theta > 380$, $|\phi| > 20°$; TTL and tropical stratosphere: $\theta > 355$ K and $|\phi| \leq 20°$; troposphere: $\theta \leq 355$ if $|\phi| \leq 20°$, or $\theta \leq \theta_{trop}$ if $|\phi| > 20°$.

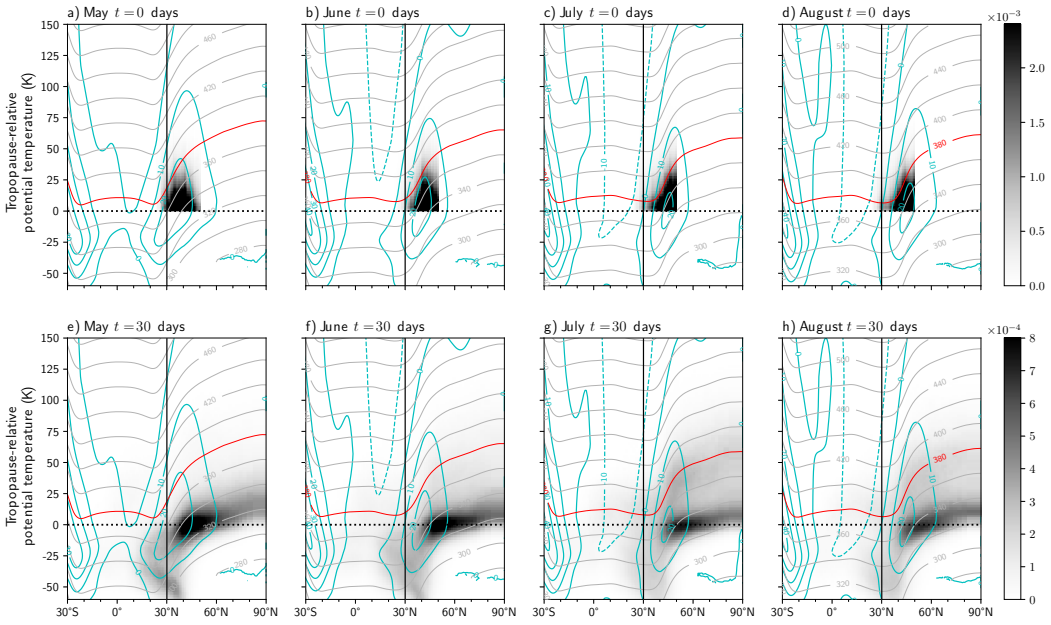

Figure 10. Normalized distributions of particles at $t = 0$ days (a, b, c, d) and $t = 30$ days (e, f, g, h) for trajectories initialized in May (a and e), June (b and f), July (c and g), and August (d and h). All distributions are normalized by the total number of particles at $t = 0$. Gray contours are isentropes, the red contour indicates the 380 K isentrope, and cyan contours are the mean zonal wind at intervals of 10 m s^{-1} (dashed negative.)

drops off quickly north of the U.S.–Canada border due to the lack of radar coverage, and this is apparent in Figures 10c and d where the high density of particle locations are cut off sharply north of 50°N. After 30 days of being advected by the large-scale flow, regardless of month, most trajectories remain in the northern hemisphere (Figures 10e–h). Note that Figures 10e–h have different color scales than those of Figures 10a–d. After 30 days of transport, trajectories from all four months exhibit a common maximum with high trajectory density centered around the tropopause in the extratropical Northern Hemisphere. This group of trajectories lies mostly around the 330 K to 350 K isentropes and above the tropopause, suggesting that these particles are mostly in the ExLMS region or in the troposphere near the tropopause.

The subtropical jet is a transport barrier between the subtropical upper troposphere and the extratropical lower stratosphere (Bowman, 1996), and as such the location of the trajectory origins relative to the subtropical jet is an important factor in determining where particles are transported. The tropopause break is the transition zone between

the high-altitude tropical tropopause and the lower extratropical tropopause, and Homeyer and Bowman (2013) used the latitude of tropopause break as the latitude of the subtropical jet. In an analysis of the dynamical tropopause, Kunz et al. (2011) show in their Figure 6 that the height of the mean subtropical jet maximum is near 350 K and that the latitudinal position of the jet core corresponds well to where the 350 K surface intersects the tropopause break. Based on these findings, in this study we evaluate the intersection of the 350 K surface and the tropopause at each 1-hourly ERA5 analysis, and use the latitudes of the intersections as the subtropical jet latitude. The jet latitude is determined at each longitude, and the jet latitude is interpolated to the trajectory initial longitude to determine the relative latitude of the trajectory initial locations with respect to the jet.

Cross-sections of particle densities in tropopause- and jet-relative coordinates are shown in Figure 11 for particles originating from north and south of the subtropical jet. After 30 days, it is observed that particles starting from south of the jet have a higher percentage remaining above the tropopause. For instance, for trajectories initialized in July north of the jet, after 30 days there are 11% above the the tropopause and south of the jet, and 28% above the tropopause and north of the jet (Figure 11g). In comparison, Figure 11o shows that the percentages are 21% and 40% for particles originating from south of the jet, indicating that it is more likely for air to stay in the stratosphere if the injection occurred south of the jet. This is true for trajectories from all four months. Since the tropopause is generally higher south of the jet, overshooting convection occurring south of the jet would inject air at higher isentropes (see Figure 10), thus favoring longer residence time in the stratosphere. The differences between the July/August versus the May/June patterns is also more notable when injections occur south of the jet. In July/August the stratospheric fractions after 30 days are significantly higher than those of May/June, suggesting that injection into the anticyclone interior (which is south of the jet) may facilitate longer residence in the stratosphere.

There is also a difference in across-jet transport among particles originating from north or south of the jet. Air from south of the jet is more likely to be mixed into north of the jet, evident from the percentages shown in Figure 11. In fact, Figure 11o and p shows that the percentages north of the jet are 52% and 53%, respectively, suggesting that air injected south of the jet in July or August is slightly more likely to be transported north of the jet. A majority of these particles are in the extratropical stratosphere.

In comparison Figure 11g and h shows that the percentages south of the jet are 36% and 27%, indicating that there is relatively less north-to-south mixing.

To further understand what determines whether CIAMs end up above or below the tropopause, we analyze the characteristics at the trajectory initial locations. The distributions of θ at $t = 0$ days for trajectories that end up above or below the tropopauses at $t = 30$ days are shown in Figure 12a . For ease of discussion we refer to the trajectory population above (below) the tropopause at $t = 30$ days as the stratospheric (tropospheric) population. The $\theta(t = 0)$ values of the stratospheric population are mostly greater than 360 K, which is not surprising given that diabatic heating is generally negative below 360 K (Figures 1–3); plumes starting below 360 K are less likely to remain in the stratosphere. However, injection above 360 K is not sufficient for plumes to remain in the stratosphere, as a large portion of the tropospheric population are characterized by $\theta(t = 0) \geq 360$ K. This suggests that factors other than injection height also play a role in causing these plumes to remain in the stratosphere. The tropopause-relative injection potential temperature is given in Figure 12b, and here the tropospheric populations are more frequently found near the tropopause than the stratospheric populations.

Figure 12c shows the initial relative vorticity of the populations. For July, the percentage of the stratospheric (tropospheric) population that has negative initial relative vorticity is 76.1% (63.5%), while for August it is 70.2% (58.6%). This suggests that there is a preference of the stratospheric population to have originated from anticyclonic flow regimes. In Figure 12d we show the distribution of Montgomery streamfunction anomaly, defined as $\psi' = \psi(\lambda_0, \phi_0, \theta_0) - \bar{\psi}(\theta_0)$ where ψ is the Montgomery streamfunction, λ_0 is the trajectory initial longitude, ϕ_0 is the trajectory initial latitude, θ_0 is the trajectory initial potential temperature, and $\bar{\psi}(\theta_0)$ is the mean Montgomery streamfunction in the domain 145°W–55°W, 10°N–55°N at θ_0. As seen in Figure 2, the anticyclone is characterized by higher values of ψ relative to the surrounding. In Figure 12d, we find that the population remaining in the stratosphere have negatively skewed distributions of ψ', with the majority of ψ' being positive. The percentage of the stratospheric (tropospheric) population with positive ψ' for July is 75.1% (34.4%) while for August it is 62.7% (24.7%). Together with Figure 12c, which shows that the stratospheric population has slightly higher probability of having originated from regions of negative vortic-

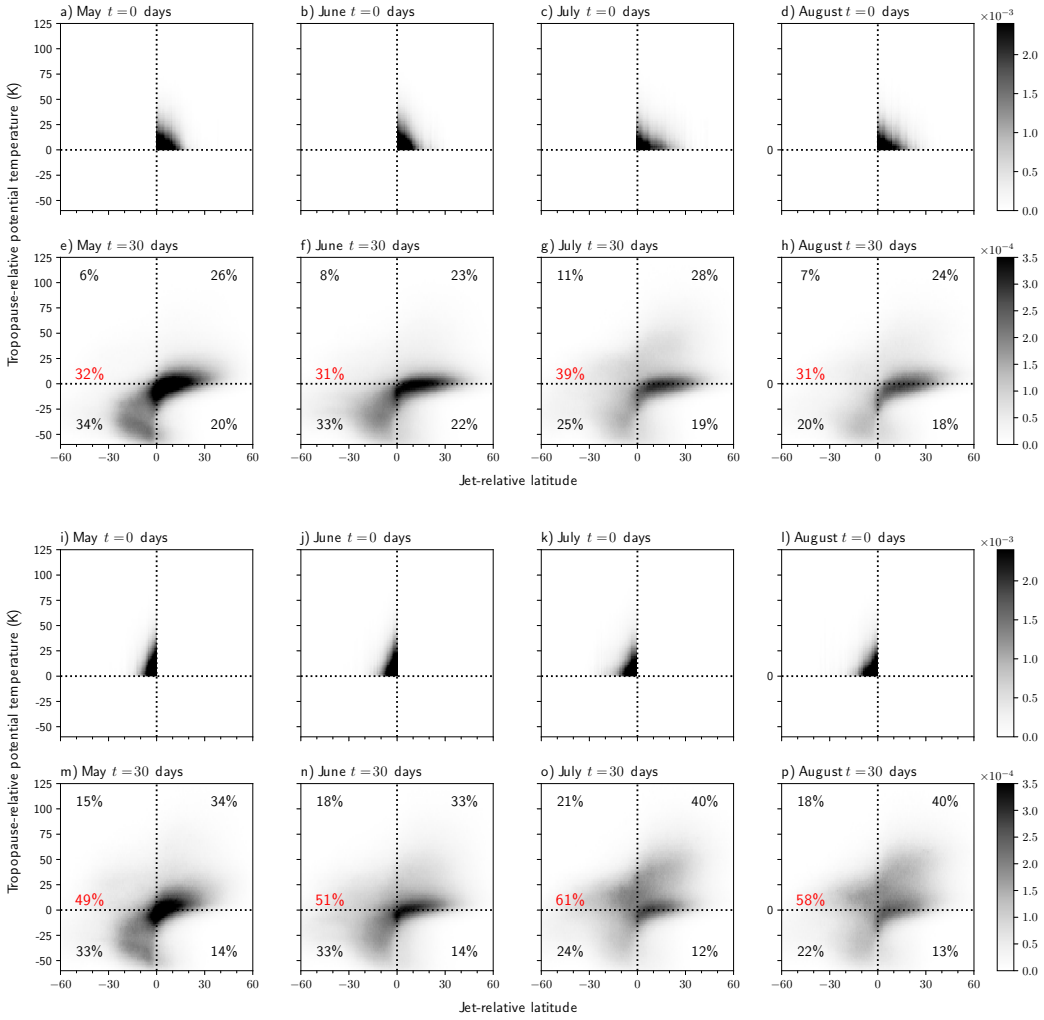

Figure 11. Normalized distributions of particles at $t = 0$ days (a, b, c, d) and $t = 30$ days (e, f, g, h) for trajectories initialized north of the subtropical jet in May (a and e), June (b and f), July (c and g), and August (d and h). In plots e–h, the percentage of trajectories in each quadrant (north/south of the jet and above/below the tropopause) are shown, and the percentages in red are the total stratospheric percentage. Plots i–p are the same as a–h except for particles originating from south of the jet.

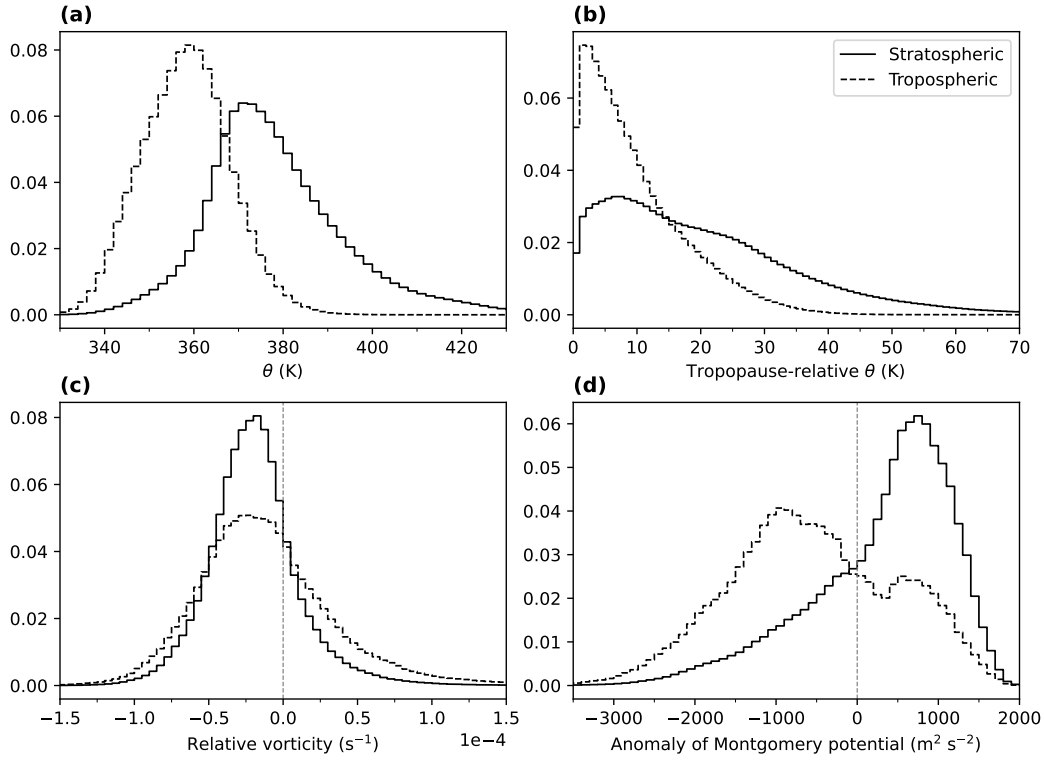

Figure 12. Normalized density functions of (a) potential temperature, (b) tropopause-relative potential temperature, (c) relative vorticity, and (d) Montgomery streamfunction anomaly at the July–August trajectory initial locations of particles from the stratospheric and tropospheric populations. The stratospheric (tropospheric) population is defined as all trajectories above (below) the tropopause after 30 days of advection. Solid (dashed) lines denote the density functions of particles from the stratospheric (tropospheric) population

ity, these two results show that convective injection into anticyclonic flow increases the chances of air plumes to remain in the stratosphere.

To examine the potential connection between the large-scale transport of CIAMs to lower stratospheric water vapor, we show the distribution of trajectories within the 90-110 hPa layer after 30 days of advection (Figure 13), overlaid with the mean 100 hPa water vapor mixing ratio based on the Aura Microwave Limb Sounder V5 H_2O product (Lambert et al., 2007). Note that in Figure 13a, while the colors show the raw count of trajectories originating from May 30 days after being spawned, the mean water vapor shown (black contours) is for June. A similar relationship applies for Figure 13b-d. The water vapor local maxima over South Asia represents the core of the Asian mon-

soon anticyclone (AMA), and we find that trajectories originating from CONUS are rarely transported into the interior of the AMA, which is consistent with large-scale divergence from the AMA. For the trajectories initialized in June, July, and August, the confinement due to the NAMA is increasingly evident, and the locations of the water vapor maxima in the western hemisphere correspond well to the regions with denser trajectories (e.g. between 20°N–40°N, 120°W–90°W in July). However, the high water vapor mixing ratios equatorward of 20°N do not generally correspond to large counts of trajectories. This suggests that additional sources of stratospheric water vapor outside the range of the U.S. NEXRAD network, such as overshooting convection occurring along the Sierra Madre Occidental in western Mexico or around the Panama Bight (Liu & Liu, 2016), may contribute to the North American water vapor feature.

4 Summary and conclusion

NEXRAD radar observations and the lapse-rate tropopause based on the ERA5 reanalysis are used to identify convective overshooting events over the CONUS during May to August over thirteen years (2008-2020). Using horizontal winds and diabatic heating rates in isentropic coordinates from ERA5, trajectory calculations are used to assess the large-scale transport of plumes originating from overshooting convection. In each grid box containing an overshooting event, particles are distributed evenly in the vertical based on pressure, so that the number of trajectories can be interpreted as proportional to the mass of convectively-influenced air. We find that the largest number of overshooting events, and thus the largest number of particles, occurs during June. Overshooting tends to occur in the central plains of the U.S., and shifts northward as the warm season proceeds from May into July/August.

We find that more overshoots and mass injection occurs during May and June, but the jet is stronger and the NAMA is non-existent or weak during these two months. As such, particles are more quickly exported from North America, particularly in May. July exhibits the strongest confinement effect on plumes from overshoots, May has the weakest, and June and August have rather comparable confinement characteristics. Following the initial rapid export from North America of a large portion of the injected air by the jet, the remaining air decreases with an e-folding time scale of around 10 days (Figure 7). Residence times over North America tend to be much longer for overshooting that occurs in the southern CONUS where the injection is much more likely to be within the

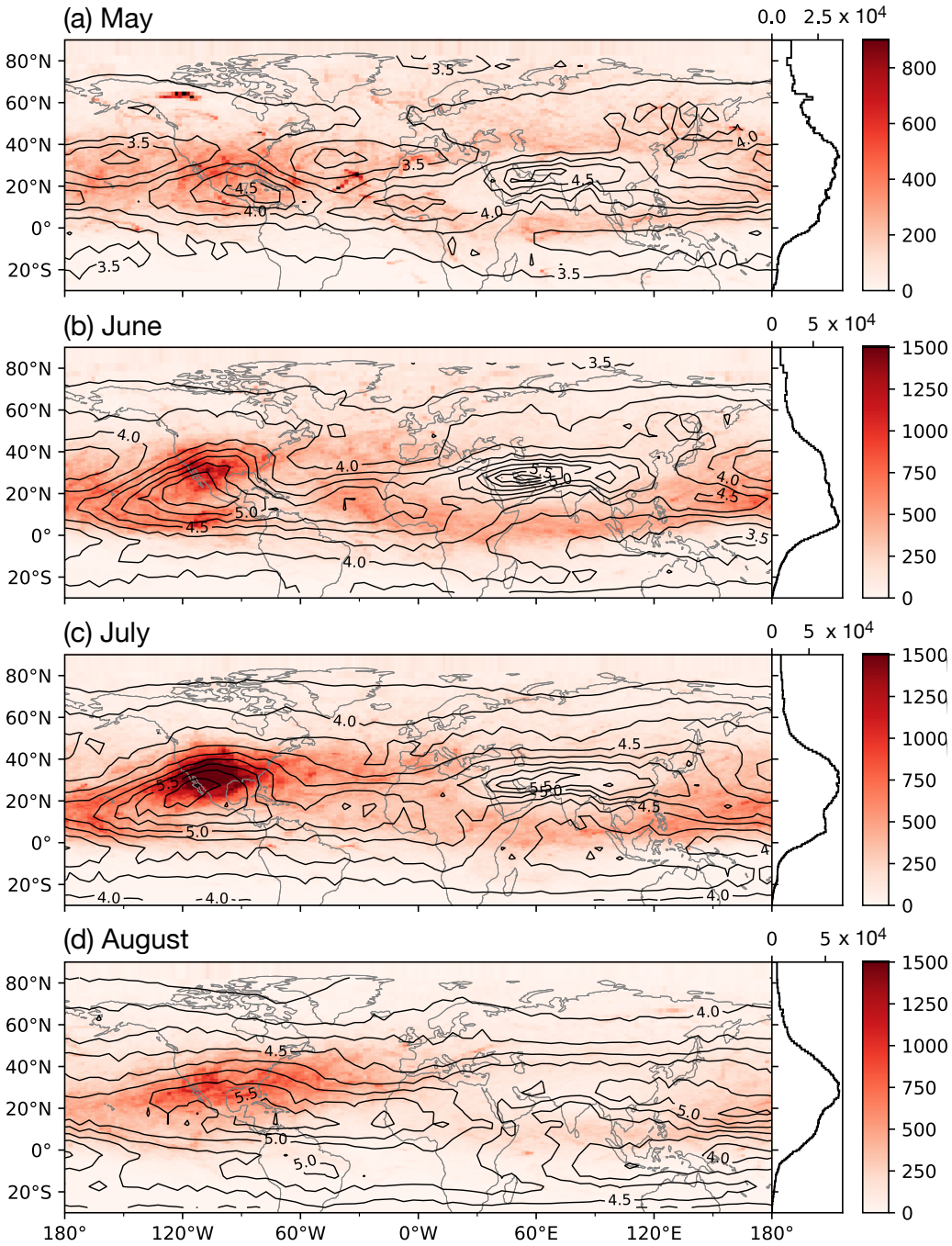

Figure 13. The raw count of trajectories (colors) within 90–110 hPa after 30 days of advection for trajectories spawned in (a) May, (b) June, (c) July, and (d) August. Black contours are the mean Aura MLS 100 hPa water vapor volume mixing ratio (ppmv) for (a) June, (b) July, (c) August, and (d) September. The right panel in each plot shows the zonally-summed trajectory count.

NAMA. This is most noticeable from July through August when the NAMA is strongest. Residence time also increases with altitude, consistent with decreasing wind speeds above the jet in the stratosphere (Figure 8).

One important question to address is how long injected air remains in the stratosphere. We show that after 30 days of transport, 45% of all particles are still in the stratosphere, and about 16% of mass is injected directly into the overworld. Transport of air from the lowermost stratosphere into the troposphere happens at a rapid and steady rate, while the loss of particles from the overworld stratosphere is much slower. For instance, the percentage of particles in July injected into the overworld stratosphere is 21%, and after 30 days of transport 17% still remain in the overworld.

By separately evaluating injection north or south of the subtropical jet, we find that a higher percentage of particles originating south of the jet stay in the stratosphere. While particles injected north of the jet can disperse above the jet in the stratosphere into the tropics, a large number descend into the troposphere north of the jet in a pattern consistent with the secondary circulation around the jet and the preferred locations of tropopause folds. As a result, a higher fraction of particles are transported into the troposphere. On the other hand, particles originating from south of the jet tends to have a higher chance of remaining in the stratosphere, especially if the injection takes place during July or August. In our analysis of trajectory initial conditions, we find that the initial potential temperature of particles and whether or not they originate within the NAMA are the best predictors of whether they will remain in the stratosphere after 30 days.

In June–August, a portion of air injected into the stratosphere over the CONUS is confined within the NAMA circulation, some descends into the troposphere, and the remainder is dispersed around the globe, mostly between 0° and 40°N. Little of the air enters the AMA circulation, consistent with the net outflow from the AMA in the lower stratosphere. Though we find correspondence between the trajectory density and western hemispheric lower stratospheric water, particularly in the subtropics and mid-latitudes, the elevated amounts of water vapor at low latitudes did not correlate to trajectories originating from CONUS. This could possibly be due to the spatial coverage of the NEXRAD, whose observations are limited mostly to the CONUS. Deep convection at lower latitudes, such as those over Gulf of Mexico, Sierre Madre, and the region around the Panama Bight, could possibly play a role in hydrating the western hemispheric lower stratosphere.

Acknowledgments

This work is funded by the National Aeronautics and Space Administration Grant 80NSSC19K0341 to Texas A&M University. ERA5 reanalysis is available from the Copernicus Climate Data Store (https://cds.climate.copernicus.eu). GridRad (Bowman & Homeyer, 2017) is available at the Research Data Archive at the National Center for Atmospheric Research at https://rda.ucar.edu/datasets/ds841.0/.

References

Anderson, J. G., Weisenstein, D. K., Bowman, K. P., Homeyer, C. R., Smith, J. B., Wilmouth, D. M., ... Wofsy, S. C. (2017, jun). Stratospheric ozone over the United States in summer linked to observations of convection and temperature via chlorine and bromine catalysis. *Proceedings of the National Academy of Sciences*, *114*(25), E4905–E4913. doi: 10.1073/pnas.1619318114

Anderson, J. G., Wilmouth, D. M., Smith, J. B., & Sayres, D. S. (2012, aug). UV Dosage Levels in Summer: Increased Risk of Ozone Loss from Convectively Injected Water Vapor. *Science*, *337*(6096), 835–839. Retrieved from `https://www.sciencemag.org/lookup/doi/10.1126/science.1222978` doi: 10.1126/science.1222978

Bowman, K. P. (1993). Large-scale isentropic mixing properties of the Antarctic polar vortex from analyzed winds. *Journal of Geophysical Research*, *98*(D12), 23013. Retrieved from `http://doi.wiley.com/10.1029/93JD02599` doi: 10.1029/93JD02599

Bowman, K. P. (1996, mar). Rossby Wave Phase Speeds and Mixing Barriers in the Stratosphere. Part I: Observations. *Journal of the Atmospheric Sciences*, *53*(6), 905–916. Retrieved from `http://journals.ametsoc.org/doi/10.1175/1520-0469(1996)053{\%}3C0905:RWPSAM{\%}3E2.0.CO;2` doi: 10.1175/1520-0469(1996)053⟨0905:RWPSAM⟩2.0.CO;2

Bowman, K. P., & Homeyer, C. R. (2017). *GridRad - Three-Dimensional Gridded NEXRAD WSR-88D Radar Data.* Boulder CO: Research Data Archive at the National Center for Atmospheric Research, Computational and Information Systems Laboratory. Retrieved from `https://doi.org/10.5065/D6NK3CR7`

Chang, K.-W., Bowman, K. P., Siu, L. W., & Rapp, A. D. (2021, jul). Convective forcing of the North American Monsoon Anticyclone at intraseasonal and in-

terannual time scales. *Journal of the Atmospheric Sciences*, *78*(3), 2941–2956. Retrieved from https://journals.ametsoc.org/view/journals/atsc/aop/JAS-D-21-0009.1/JAS-D-21-0009.1.xml doi: 10.1175/JAS-D-21-0009.1

Clapp, C. E., Smith, J. B., Bedka, K. M., & Anderson, J. G. (2019). Identifying Source Regions and the Distribution of Cross-Tropopause Convective Outflow Over North America During the Warm Season. *Journal of Geophysical Research: Atmospheres*, 1–13. doi: 10.1029/2019JD031382

Clapp, C. E., Smith, J. B., Bedka, K. M., & Anderson, J. G. (2021, may). Identifying Outflow Regions of North American Monsoon Anticyclone-Mediated Meridional Transport of Convectively Influenced Air Masses in the Lower Stratosphere. *Journal of Geophysical Research: Atmospheres*, *126*(10), 1–19. Retrieved from https://onlinelibrary.wiley.com/doi/10.1029/2021JD034644 doi: 10.1029/2021JD034644

Cooney, J. W., Bowman, K. P., Homeyer, C. R., & Fenske, T. M. (2018). Ten Year Analysis of Tropopause-Overshooting Convection Using GridRad Data. *Journal of Geophysical Research: Atmospheres*, *123*(1), 329–343. doi: 10.1002/2017JD027718

Corti, T., Luo, B. P., de Reus, M., Brunner, D., Cairo, F., Mahoney, M. J., ... Peter, T. (2008). Unprecedented evidence for deep convection hydrating the tropical stratosphere. *Geophysical Research Letters*, *35*(10), 1–5. doi: 10.1029/2008GL033641

de Reus, M., Borrmann, S., Bansemer, A., Heymsfield, A. J., Weigel, R., Schiller, C., ... Ravegnani, F. (2009, sep). Evidence for ice particles in the tropical stratosphere from in-situ measurements. *Atmospheric Chemistry and Physics*, *9*(18), 6775–6792. Retrieved from https://acp.copernicus.org/articles/9/6775/2009/ doi: 10.5194/acp-9-6775-2009

Dessler, A. E., & Sherwood, S. C. (2004, dec). Effect of convection on the summertime extratropical lower stratosphere. *Journal of Geophysical Research: Atmospheres*, *109*(D23), 1–9. Retrieved from http://doi.wiley.com/10.1029/2004JD005209 doi: 10.1029/2004JD005209

Dethof, A., O'Neill, A., Slingo, J. M., & Berrisford, P. (2000, aug). Quantification of isentropic water-vapour transport into the lower stratosphere. *Quarterly Journal of the Royal Meteorological Society*, *126*(566), 1771–1788.

Retrieved from http://doi.wiley.com/10.1002/qj.49712656611 doi: 10.1002/qj.49712656611

Fischer, H., de Reus, M., Traub, M., Williams, J., Lelieveld, J., de Gouw, J., ... Siegmund, P. (2003, jun). Deep convective injection of boundary layer air into the lowermost stratosphere at midlatitudes. *Atmospheric Chemistry and Physics*, *3*(3), 739–745. Retrieved from https://acp.copernicus.org/articles/3/739/2003/ doi: 10.5194/acp-3-739-2003

Forster, P. M. D. F., & Shine, K. P. (2002, mar). Assessing the climate impact of trends in stratospheric water vapor. *Geophysical Research Letters*, *29*(6), 10–1–10–4. Retrieved from http://doi.wiley.com/10.1029/2001GL013909 doi: 10.1029/2001GL013909

Hanisco, T. F., Moyer, E. J., Weinstock, E. M., St. Clair, J. M., Sayres, D. S., Smith, J. B., ... Bui, T. P. (2007, feb). Observations of deep convective influence on stratospheric water vapor and its isotopic composition. *Geophysical Research Letters*, *34*(4), L04814. Retrieved from http://doi.wiley.com/10.1029/2006GL027899 doi: 10.1029/2006GL027899

Herman, R. L., Ray, E. A., Rosenlof, K. H., Bedka, K. M., Schwartz, M. J., Read, W. G., ... Dean-Day, J. M. (2017). Enhanced stratospheric water vapor over the summertime continental United States and the role of overshooting convection. *Atmospheric Chemistry and Physics*, *17*(9), 6113–6124. doi: 10.5194/acp-17-6113-2017

Hersbach, H., Bell, B., Berrisford, P., Hirahara, S., Horányi, A., Muñoz-Sabater, J., ... Thépaut, J. (2020, jul). The ERA5 global reanalysis. *Quarterly Journal of the Royal Meteorological Society*, *146*(730), 1999–2049. doi: 10.1002/qj.3803

Homeyer, C. R., & Bowman, K. P. (2013). Rossby wave breaking and transport between the tropics and extratropics above the subtropical jet. *Journal of the Atmospheric Sciences*, *70*(2), 607–626. doi: 10.1175/JAS-D-12-0198.1

Hossaini, R., Chipperfield, M. P., Montzka, S. A., Leeson, A. A., Dhomse, S. S., & Pyle, J. A. (2017). The increasing threat to stratospheric ozone from dichloromethane. *Nature Communications*, *8*(May), 1–9. Retrieved from http://dx.doi.org/10.1038/ncomms15962 doi: 10.1038/ncomms15962

Hossaini, R., Chipperfield, M. P., Montzka, S. A., Rap, A., Dhomse, S., & Feng, W. (2015, mar). Efficiency of short-lived halogens at influencing climate through

depletion of stratospheric ozone. *Nature Geoscience*, *8*(3), 186–190. Retrieved from `http://www.nature.com/articles/ngeo2363` doi: 10.1038/ngeo2363

Jensen, E. J., Pan, L. L., Honomichl, S., Diskin, G. S., Krämer, M., Spelten, N., ... Smith, J. B. (2020). Assessment of Observational Evidence for Direct Convective Hydration of the Lower Stratosphere. *Journal of Geophysical Research: Atmospheres*, *125*(15), 1–12. doi: 10.1029/2020JD032793

Kunz, A., Konopka, P., Müller, R., & Pan, L. L. (2011). Dynamical tropopause based on isentropic potential vorticity gradients. *Journal of Geophysical Research Atmospheres*, *116*(1), 1–13. doi: 10.1029/2010JD014343

Lambert, A., Read, W. G., Livesey, N. J., Santee, M. L., Manney, G. L., Froidevaux, L., ... Atlas, E. (2007, dec). Validation of the Aura Microwave Limb Sounder middle atmosphere water vapor and nitrous oxide measurements. *Journal of Geophysical Research*, *112*(D24), D24S36. Retrieved from `http://doi.wiley.com/10.1029/2007JD008724` doi: 10.1029/2007JD008724

Legras, B., & Bucci, S. (2020). Confinement of air in the Asian monsoon anticyclone and pathways of convective air to the stratosphere during the summer season. *Atmospheric Chemistry and Physics*, *20*(18), 11045–11064. doi: 10.5194/acp-20-11045-2020

Li, Q. (2005). North American pollution outflow and the trapping of convectively lifted pollution by upper-level anticyclone. *Journal of Geophysical Research*, *110*(D10), D10301. Retrieved from `http://doi.wiley.com/10.1029/2004JD005039` doi: 10.1029/2004JD005039

Li, Q., Jiang, J. H., Wu, D. L., Read, W. G., Livesey, N. J., Waters, J. W., ... Jacob, D. J. (2005, jul). Convective outflow of South Asian pollution: A global CTM simulation compared with EOS MLS observations. *Geophysical Research Letters*, *32*(14), n/a–n/a. Retrieved from `http://doi.wiley.com/10.1029/2005GL022762` doi: 10.1029/2005GL022762

Liu, N., & Liu, C. (2016). Global distribution of deep convection reaching tropopause in 1 year GPM observations. *Journal of Geophysical Research*, *121*(8), 3824–3842. doi: 10.1002/2015JD024430

Nielsen, J. K., Larsen, N., Cairo, F., Di Donfrancesco, G., Rosen, J. M., Durry, G., ... Pommereau, J. P. (2007, feb). Solid particles in the tropical lowest stratosphere. *Atmospheric Chemistry and Physics*, *7*(3), 685–695. Re-

trieved from https://acp.copernicus.org/articles/7/685/2007/ doi: 10.5194/acp-7-685-2007

Park, M., Randel, W. J., Emmons, L. K., Bernath, P. F., Walker, K. A., & Boone, C. D. (2008, feb). Chemical isolation in the Asian monsoon anticyclone observed in Atmospheric Chemistry Experiment (ACE-FTS) data. *Atmospheric Chemistry and Physics*, *8*(3), 757–764. Retrieved from https://acp.copernicus.org/articles/8/757/2008/ doi: 10.5194/acp-8-757-2008

Park, M., Randel, W. J., Gettelman, A., Massie, S. T., & Jiang, J. H. (2007, aug). Transport above the Asian summer monsoon anticyclone inferred from Aura Microwave Limb Sounder tracers. *Journal of Geophysical Research*, *112*(D16), D16309. Retrieved from http://doi.wiley.com/10.1029/2006JD008294 doi: 10.1029/2006JD008294

Poulida, O., Dickerson, R. R., & Heymsfield, A. (1996, mar). Stratosphere-troposphere exchange in a midlatitude mesoscale convective complex: 1. Observations. *Journal of Geophysical Research: Atmospheres*, *101*(D3), 6823–6836. Retrieved from http://doi.wiley.com/10.1029/95JD03523 doi: 10.1029/95JD03523

Randel, W. J., Park, M., Emmons, L., Kinnison, D., Bernath, P., Walker, K. A., ... Pumphrey, H. (2010, apr). Asian Monsoon Transport of Pollution to the Stratosphere. *Science*, *328*(5978), 611–613. doi: 10.1126/science.1182274

Schwartz, M. J., Read, W. G., Santee, M. L., Livesey, N. J., Froidevaux, L., Lambert, A., & Manney, G. L. (2013). Convectively injected water vapor in the North American summer lowermost stratosphere. *Geophysical Research Letters*, *40*(10), 2316–2321. doi: 10.1002/grl.50421

Siu, L. W., & Bowman, K. P. (2019). Forcing of the upper-tropospheric monsoon anticyclones. *Journal of the Atmospheric Sciences*, *76*(7), 1937–1954. doi: 10.1175/JAS-D-18-0340.1

Smith, J. B., Wilmouth, D. M., Bedka, K. M., Bowman, K. P., Homeyer, C. R., Dykema, J. A., ... Anderson, J. G. (2017, sep). A case study of convectively sourced water vapor observed in the overworld stratosphere over the United States. *Journal of Geophysical Research: Atmospheres*, *122*(17), 9529–9554. Retrieved from https://onlinelibrary.wiley.com/doi/10.1002/2017JD026831 doi: 10.1002/2017JD026831

Solomon, S., Rosenlof, K. H., Portmann, R. W., Daniel, J. S., Davis, S. M., Sanford, T. J., & Plattner, G.-K. (2010, mar). Contributions of Stratospheric Water Vapor to Decadal Changes in the Rate of Global Warming. *Science*, *327*(5970), 1219–1223. Retrieved from `http://www.sciencemag.org/cgi/doi/10.1126/science.1182488https://www.sciencemag.org/lookup/doi/10.1126/science.1182488` doi: 10.1126/science.1182488

Tinney, E. N., & Homeyer, C. R. (2021, feb). A 13-year Trajectory-Based Analysis of Convection-Driven Changes in Upper Troposphere Lower Stratosphere Composition Over the United States. *Journal of Geophysical Research: Atmospheres*, *126*(3), 1–31. Retrieved from `https://onlinelibrary.wiley.com/doi/10.1029/2020JD033657` doi: 10.1029/2020JD033657

Ungermann, J., Ern, M., Kaufmann, M., Müller, R., Spang, R., Ploeger, F., ... Riese, M. (2016). Observations of PAN and its confinement in the Asian summer monsoon anticyclone in high spatial resolution. *Atmospheric Chemistry and Physics*, *16*(13), 8389–8403. doi: 10.5194/acp-16-8389-2016

Vernier, J. P., Fairlie, T. D., Natarajan, M., Wienhold, F. G., Bian, J., Martinsson, B. G., ... Bedka, K. M. (2015). Increase in upper tropospheric and lower stratospheric aerosol levels and its potential connection with Asian pollution. *Journal of Geophysical Research*, *120*(4), 1608–1619. doi: 10.1002/2014JD022372

Werner, F., Schwartz, M. J., Livesey, N. J., Read, W. G., & Santee, M. L. (2020). Extreme Outliers in Lower Stratospheric Water Vapor Over North America Observed by MLS: Relation to Overshooting Convection Diagnosed From Colocated Aqua-MODIS Data. *Geophysical Research Letters*, *47*(24). doi: 10.1029/2020GL090131

WMO. (1957). Definition of the tropopause. *WMO Bull.*, *6*, 136.

Yan, X., Konopka, P., Ploeger, F., Podglajen, A., Wright, J. S., Müller, R., & Riese, M. (2019, dec). The efficiency of transport into the stratosphere via the Asian and North American summer monsoon circulations. *Atmospheric Chemistry and Physics*, *19*(24), 15629–15649. Retrieved from `https://acp.copernicus.org/articles/19/15629/2019/` doi: 10.5194/acp-19-15629-2019

Yu, W., Dessler, A. E., Park, M., & Jensen, E. J. (2020). Influence of con-

650 vection on stratospheric water vapor in the North American monsoon re-
651 gion. *Atmospheric Chemistry and Physics*, *20*(20), 12153–12161. doi:
652 10.5194/acp-20-12153-2020